COMPUTATIONAL STUDY OF OXYGEN REDUCTION REACTION ON CO-FUNCTIONALIZED PORPHYRIN-LIKE GRAPHENE

by

Sizhe Peng

Bachelor of Engineering, Beijing Institute of Technology, 2016

Submitted to the Graduate Faculty of

Swanson School of Engineering in partial fulfillment

of the requirements for the degree of

Master of Science

University of Pittsburgh

2018

UNIVERSITY OF PITTSBURGH

SWANSON SCHOOL OF ENGINEERING

This thesis was presented

by

Sizhe Peng

It was defended on

July 24, 2018

and approved by

Guofeng Wang, Ph.D., Associate Professor

Department of Mechanical Engineering and Materials Science

John Keith, Ph.D., Assistant Professor

Department of Chemical and Petroleum Engineering

Lei Li, Ph.D., Associate Professor

Department of Chemical and Petroleum Engineering

Thesis Advisor: Guofeng Wang, Ph.D., Associate Professor

Department of Mechanical Engineering and Materials Science

COMPUTATIONAL STUDY OF OXYGEN REDUCTION REACTION ON CO-FUNCTIONALIZED PORPHYRIN-LIKE GRAPHENE

Sizhe Peng, M.S

University of Pittsburgh, 2018

The application of proton exchange membrane fuel cells (PEMFCs), using an abundant, efficient and clean energy source of hydrogen, is highly limited by its current requirement of precious Pt-based electrode materials. An alternative to solve this problem is to replace them by transition metal/nitrogen doped carbon-based materials (TM-N/C). The performance of the new materials is not as good as that of Pt-based materials but very close, and their price is much lower.

In this study, the first-principles density functional theory (DFT) calculations are employed to study the true nature of active sites and the effect of varied N atoms number to the oxygen reduction reaction (ORR) on Co-N/C materials. OOH dissociation and O-OH reduction is also investigated as elemental reactions of ORR. The transition state and active energy of OOH dissociation is obtained by climbing-image nudged elastic band (Cl-NEB) method.

The possible active site is assumed planar Co-N_x clusters embedded in graphene. Adsorption energy calculation shows that the lack of surrounding N atoms strengthens the adsorption of all ORR species on Co-N_x clusters and leads to a remarkably strong adsorption on their bridge site. Further investigation suggests that such strong adsorption on bridge site could decrease the active energy required by OOH dissociation and change the limiting elemental reaction.

After the analyses of the free energy landscapes of $4e^-$ and $2e^-$ ORR on all possible CoN_x clusters, one of them shows a strong possibility acting as the active site of $4e^-$ ORR. The active energy of OOH dissociation is 0.78eV and the limiting potential is 0.42V, which is very close to the property of Pt. Besides, $2e^-$ ORR research gives a limiting potential of 0.47V, suggesting an acceptable selectivity of the cluster as a $4e^-$ ORR catalytic site.

TABLE OF CONTENTS

LIST OF TABLES

LIST OF FIGURES

ACKNOWLEDGMENTS

Grateful acknowledgement is given to my advisor, Dr. Guofeng Wang for his two-year patience, teaching and guiding.

Grateful acknowledgement is given to my co-worker, Dr. Kexi Liu, Dr. Zhenyu Liu, Dr. Siming Zhang and Dr. Boyang Li for their great support to my research.

1.0 INTRODUCTION

Energy has always been a crucial factor for social progression. In the last two centuries, human world has developed dramatically due to several industrial revolutions, so has global energy consumption[1,2]. Most of those energy were obtained from coal, oil, and natural gas[3,4]. However fossil fuel is questioned by serious environmental issues, and it`s reported to be depleted in few decades or centuries[5]. Therefore, a completely new energy system with clean, renewable energy source is needed.

An alternative of the new energy source is hydrogen. Hydrogen is widely distributed in the world, especially in the form of water in ocean, which covers 72% of the earth surface. Thus, hydrogen can be easily acquired from water by electrolysis. Formed by the lightest element in the periodic table, hydrogen gas has the least molecular weight, yet it contains much chemical energy. The oxidation of hydrogen gives out an energy of 285.83kJ/mol (liquid water), showing the high energy density of hydrogen. Moreover, while the combustion of fossil fuel produces greenhouse gases like carbon oxide, nitrogen oxide and sulfur oxide, the oxidation of hydrogen only leads to water, which is totally clean and environmental friendly. Tough there exists some technical difficulties of the application of hydrogen, it is still a promising energy source in the future.

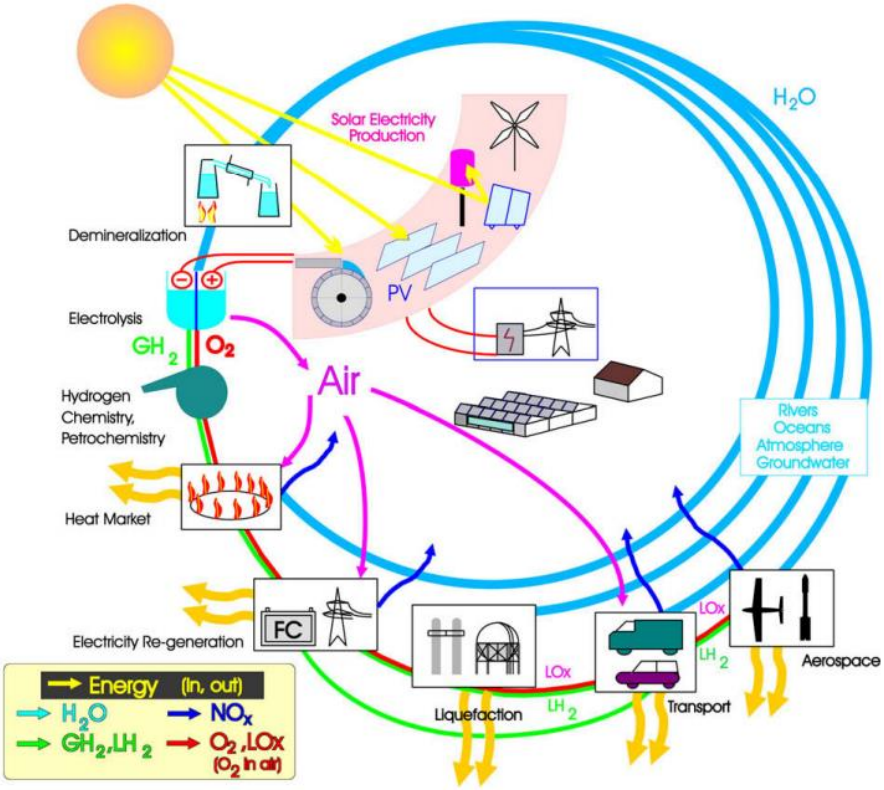

Figure 1. Materially closed hydrogen energy systems.

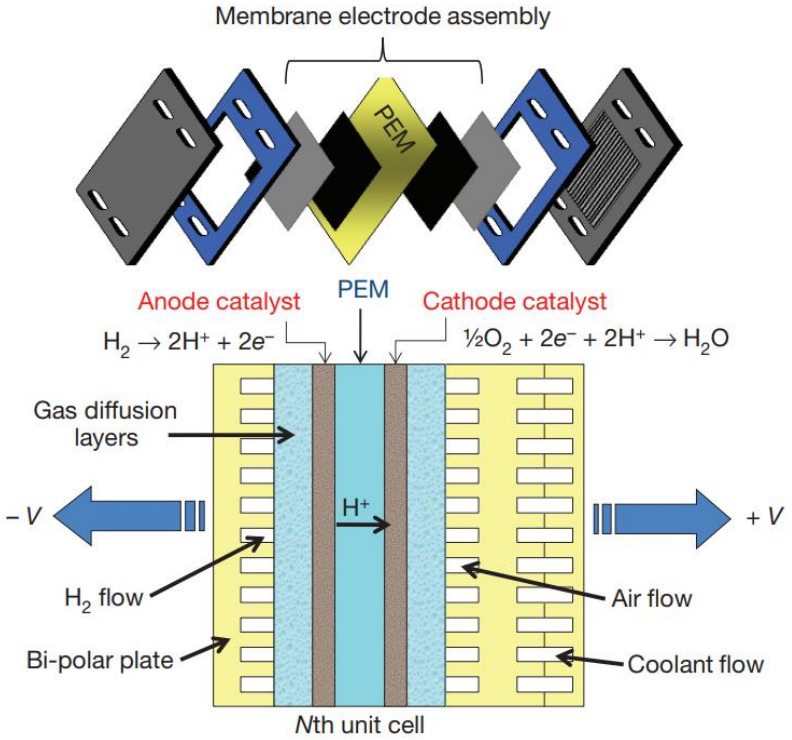

Figure 2. PEMFC components (from ref 6).

The application of proton exchange membrane fuel cells(PEMFCs), utilizing an abundant, efficient, and clean energy source of hydrogen[7], is a promising option to alleviate the social problems mentioned above. Compared to other fuel cells, the vital advantage of PMEFCs is its relatively low working temperature, which allows PEMFCs to operate in a normal condition[8]. The components of PEMFCs and the electrode reactions are demonstrated in Figure 2. Hydrogen evolution happens on the anode and the oxygen reduction reaction occurs on the cathode. the electrodes serve as catalysts of all reactions on its surface, so one measure to optimize the fuel cell is to advance the catalyst material technology. To be widely applied on all mobile devices, fuel cells need to be cheap enough. However, the large scale commercial application of PEMFCs is currently restricted by their precious Pt group electrocatalyst materials[9]. To be widely applied on all mobile devices, fuel cells need to be cheap enough, which is violated by the price of the precious Pt-based materials. In this regard, the non-precious transition metal/nitrogen doped carbon based(TM-N/C) materials are widely studied to replace Pt, in particular, the precious Pt based cathode materials, where oxygen reduction reaction(ORR) takes place[10].

The application of TM/N/C materials is initially reported in 1964 that cobalt phthalocyanine(CoPc) could act as ORR electrocatalyst in alkaline conditions[11], followed by the discovery of catalytic activity of various TM-N_4/C materials(for example, FePc, which is shown in Figure 3) in acid media. The stability issue was solved when heat treatment procedures were introduced to the catalyst synthesis process, which increases the concentration of active ORR active sites, and improves the stability as well[12,13].

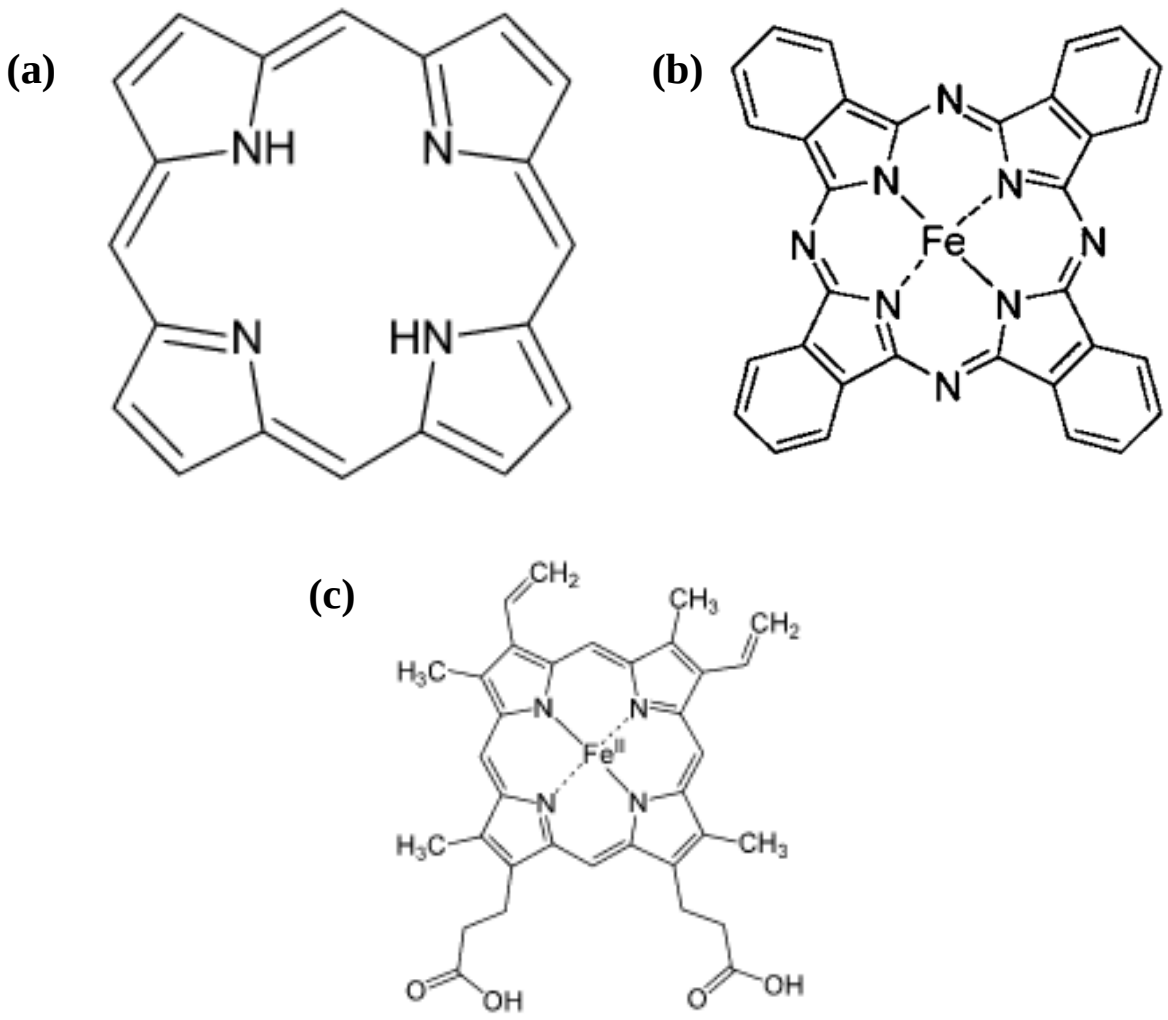

Figure 3. Molecular structures of **(a)** porphyrin, **(b)** FePc, and **(c)** heme B. Most of TM functionalized porphyrin-like structure shows the ability of strong O_2 adsorption.

Recent experimental study showed that the catalytic activity of the electrodes made from pyrolyzed TM-N/C materials for ORR could match with that of the electrode made from pure Pt in alkaline media[14,15] , acid media[16,17,18], and membrane electrode assembly[19,20]. Those TM/N/C materials are typically synthesized by mixing metal and nitrogen precursor with supporting carbon materials (for example, carbon nanotube, carbon nanoparticle, graphene, and high specific area carbon) and then heat-treating the mixture in specific environment (such as high temperature and insert gases). The ORR catalytic performance of TM/N/C materials is basically optimized by varying the ratio and chemical species of the metal and nitrogen precursors, or the type of carbon materials[20].

A recent research gave out the idea that the catalytic performance of TM-N/C could be very close to Pt, given by certain synthesis methods. According to Figure 4.a, the onset potentials of Pt and Co-N/C materials were about 0.95V and 0.85V respectively. Moreover, the current densities of the two materials at high rotating rate is nearly the same. All evidence indicates that the performance of TM-N/C materials for ORR is every close to that of Pt materials, while its price is much lower than the price of Pt. This suggests that TM-N/C is a promising material to replace the precious Pt in PEMFCs[21].

The physical structures of the samples are first tested with several characterization methods (such as scanning electron microscope and X-ray photoelectron spectroscopy). The electrochemical properties are measured in three-electrode system, especially in rotating ring-disk electrode system to reduce the effect of polarization on catalyst surface[17].

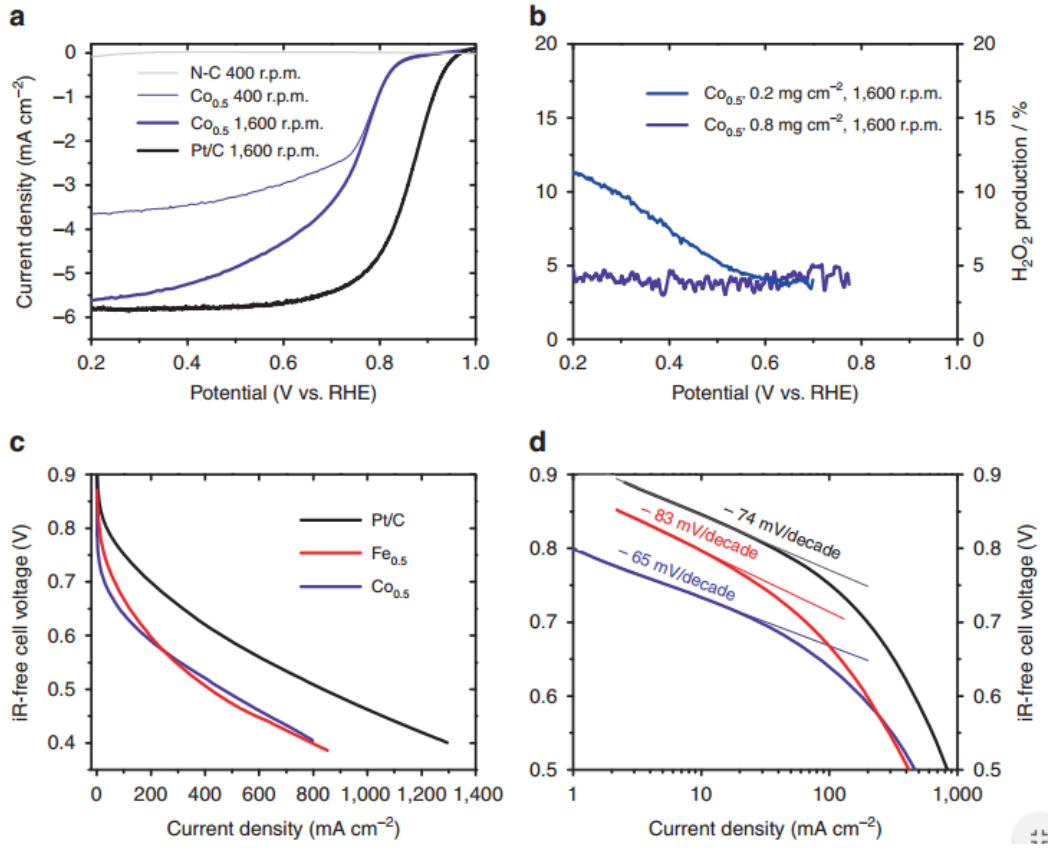

Figure 4. ORR electrochemical characterization measurements of Co0.5, Fe0.5, N-C and a Pt/C benchmark catalyst. Upper panels are RRDE measurements at various rotation rates and loadings performed in O2-saturated 0.1 M H2SO4 aqueous solution. **a** ORR current density at the disk. **b** % H2O2 measured during ORR at the ring. Lower panels are iR-corrected PEMFC polarization curves with Co0.5, Fe0.5 or Pt/C at the cathode, presented in linear scale **c** and semi-logarithmic scale **d**. There results are from ref 21.

Figure 5. Spectroscopic mapping of iron and nitrogen atoms on carbon nanotube–graphene complexes. (a) nitrogen Electron Energy Loss Spectroscopy (EELS) mapping, (b) iron EELS mapping, (c) An overlaid iron and nitrogen EELS map. The ADF and EELS maps were recorded simultaneously. Interestingly, iron atoms are frequently observed on the edges of graphene sheets near nitrogen species (from ref 17).

In physical studies of the catalyst surface, it is presumed that some transition metal-nitrogen (TM-N_x) clusters are formed on the catalyst surface by the heat treatment (shown in Figure 5), and these clusters are considered responsible for the ORR catalytic activity of TM-N/C materials. Such conclusion is also supported by the atomic structure of heme B, which carries the oxygen in blood. The similar structure of metal-functionalized porphyrin is discovered extensively in natural organisms, playing the role related to oxygen. Thus, the active site of TM-N/C material is supposed to be similar with FePc.

1.1 REACTION MECHANISM

Oxygen reduction reaction is a series of sub-reactions occurring on the cathode of oxygen-based fuel cells. The series is assumed containing a sequential addition of a proton and electron in each elementary reaction and one oxygen bond dissociation, yet the order of those reaction varies from the active sites[22,23].

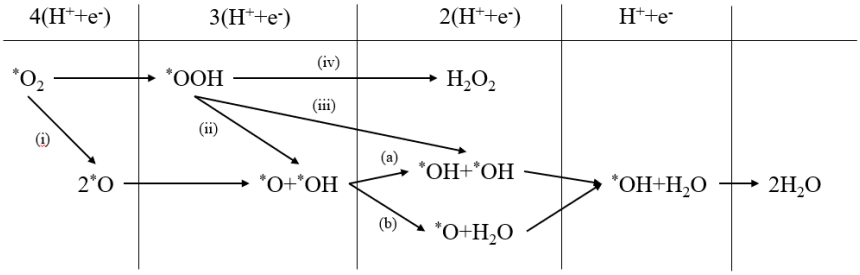

Figure 6. All possible pathways of ORR. (i)O_2 dissociation. (ii)OOH dissociation. (iii)HOOH dissociation. (iv) $2e^-$-pathway. (a)Reaction to form two *OH. (b)Reaction to form *O and H_2O.

The three major pathways (demonstrated as (i), (ii)and(iii)in Figure 4), O2 dissociation, OOH dissociation, and HOOH dissociation are distinguished by the oxygen bond dissociation (Figure 6). The choice of reaction pathways depends on the electrocatalyst materials. For example, the O2 dissociation reaction was thermodynamically feasible in some DFT calculations for metallic electrocatalyst materials[22]. Some other DFT studies claimed that the ORR on FeN4 cluster prefers OOH dissociation among all three major possible pathways[24,25, 26].

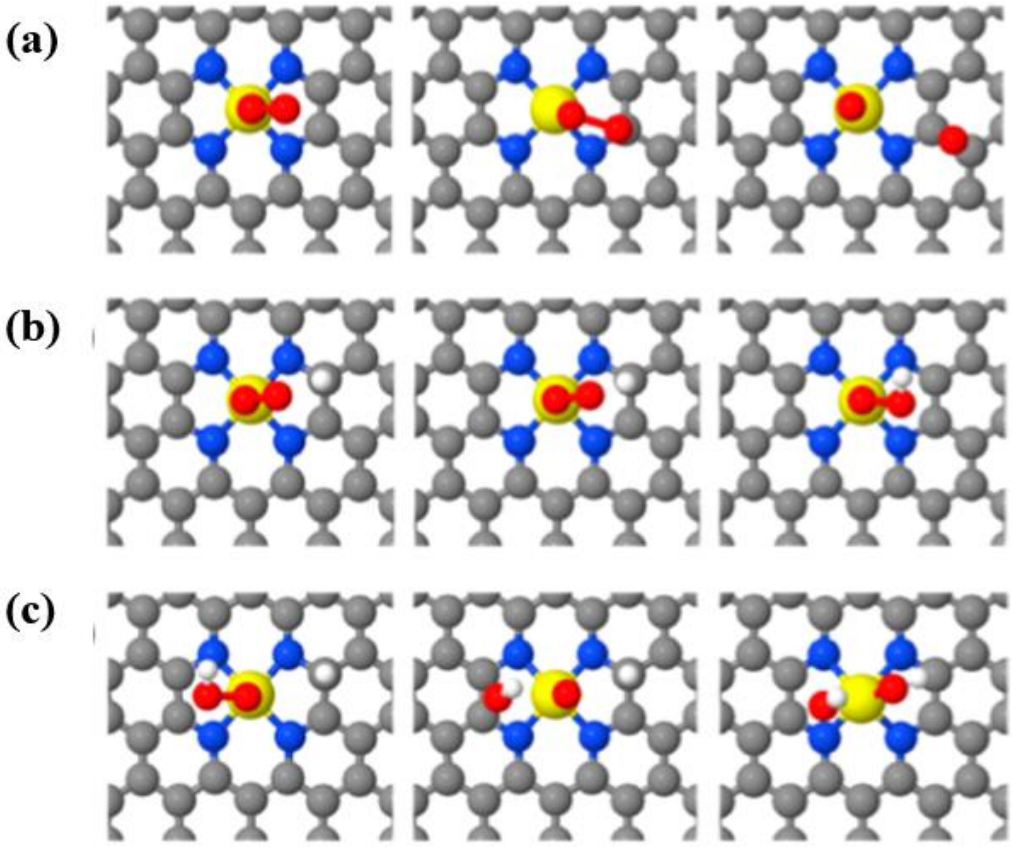

Figure 7. Atomic structures of the initial state (left panel), transition state (middle panel), and final state (right panel) for (a) O2 dissociation, (b) OOH dissociation, (c) HOOH dissociation, reactions on FeN4 embedded graphene. In the figure, the gray, blue, yellow, red, and white balls represent C, N, Fe, O, and H atoms, respectively.

Another pathway separation occurs at O-OH reduction (shown as (a) and (b) in Figure 5), where the reaction is splitted into 2OH route and O-H2O route distinguished by which oxygen to be reduced in O-OH system. To understand the specific mechanism of ORR, the O-OH reduction was investigated in some DFT studies[27] (Figure 8).

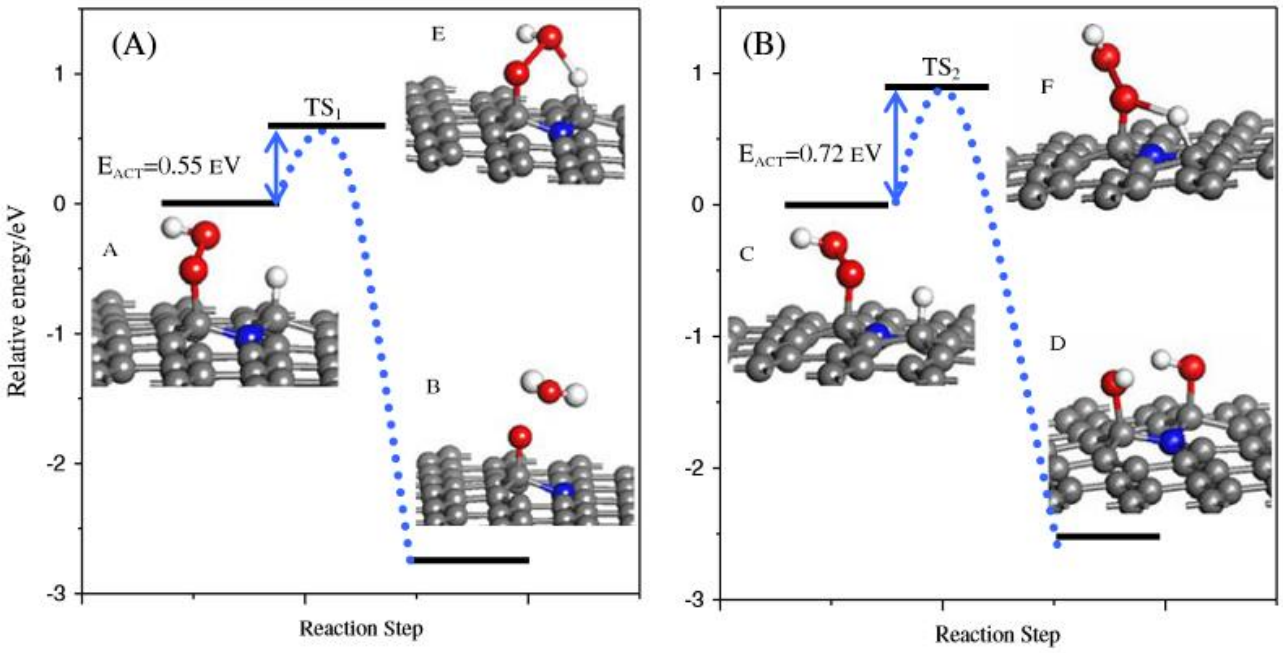

Figure 8. Relative reaction energy and activation barrier of OOH reduction on surface together with optimized reactant and product structures and corresponding transition structures. A Reduction to form *O and H_2O. B Reduction to form 2*OH[28].

Neither the 2OH route nor the O-H_2O route were reported in experimental studies. This calculation was conducted only to figure out the mechanism of O-OH reduction and to decide the reactants of later reactions.

Some experimental studies found that the number of transferred electrons of ORR was less than the expected number of 4, suggesting that despite of all $4e^-$-pathways, there exists a $2e^-$-pathway in which the oxygen bond doesn`t break (exhibited as (iv)in Figure 6), and this H_2O_2 producing reaction is a side reaction on PEMFCs cathodes, and highly competitive to $4e^-$-pathway reaction. Therefore, the catalytic activity for $2e^-$-pathway reaction of an ideal cathode material is supposed as low as possible. As an important factor to measure the selectivity of an ORR electrocatalyst, the $2e^-$-pathway analyze is included in most of ORR material studies. Several DFT studies have found that the H_2O_2 adsorption on ORR catalyst is relatively weak comparing to other ORR species. In some cases, the H_2O_2 adsorption doesn`t exist. These conclusions indicate that the $2e^-$-pathway is also energetical favorable in addition with the calculation of the low activate energy for H_2O_2 production (Figure 9), well explaining the experimental results mentioned above[18, 28].

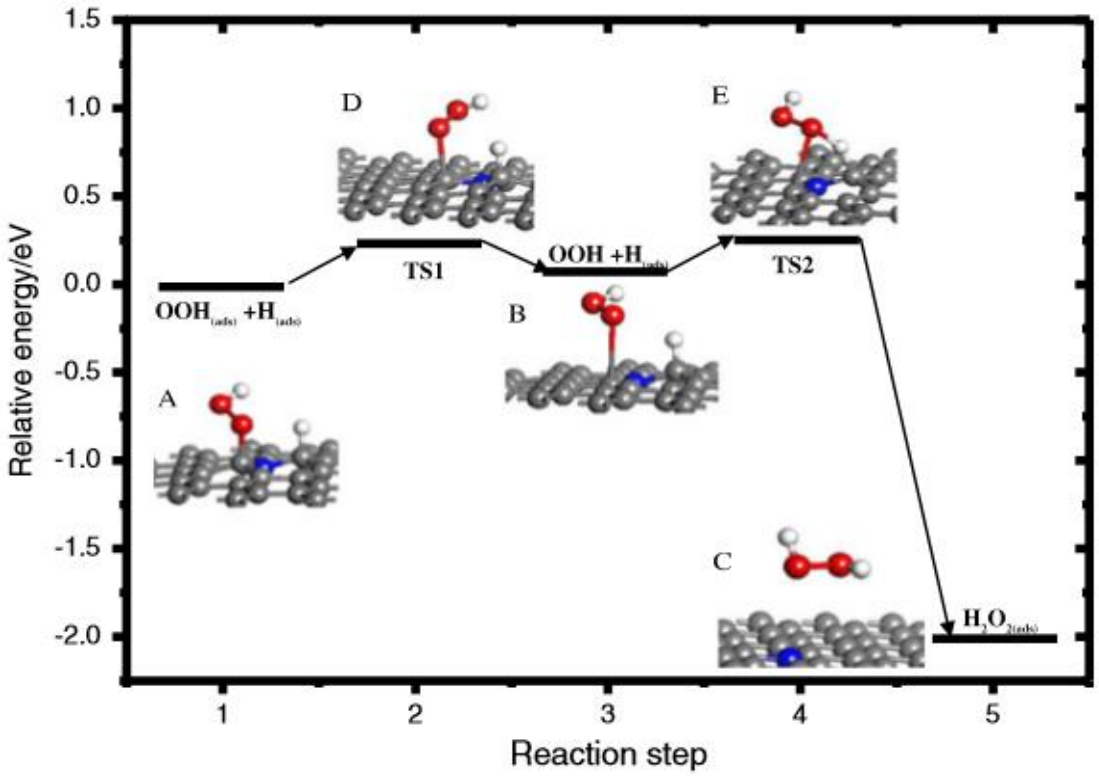

Figure 9. Relative reaction energy and activation barrier of OOH reduction to form H2O2 on N doped graphene surface together with optimized reactant and product structures and corresponding transition structures. A Adsorbed OOH and H species. B Stably adsorbed H and desorbed OOH. C Generated H2O2. D and E are the two corresponding transition states (from ref 28).

1.2 PREVIOUS RESULTS

The researches of Co-N/C materials were conducted both experimentally and computationally. In experimental study, the material was first synthesized from certain precursors under certain conditions. Then the material was tested in electrochemical devices such as rotating electrode (RDE). In further research, the PEMFC containing the material was tested. As a catalyst for ORR, Co-N/C materials were judged by its activity, selectivity and durability. To explain the activity and the selectivity given by experimental measurements, computational studies were introduced. Computational studies started with initial assumptions of the active sites on Co-N/C materials, ended with the predictions of certain properties of the sites. By matching the predictions to the experimental results, computational methods could investigate the true nature of the active sites.

The selectivity of a Co-N/C material is judged by comparing the activity of $4e^-$ ORR to that of $2e^-$ ORR, which is the site reaction producing H_2O_2. This can be easily achieved by measure the number of electron transferred(n). n is calculated by Koutecky-Levich equation, which demonstrates the relationship between the current density and the rotating rate in RDE measurement:

$$\frac{1}{J} = \frac{1}{J_L} + \frac{1}{J_K} = \frac{1}{B\omega^{1/2}} + \frac{1}{J_K}$$

$$B = 0.62nFC_0D_0^{2/3}\nu^{-1/6};\ J_K = nFkC_0$$

If n=2, only $2e^-$ ORR occurs on the material. If n=4, only $4e^-$ ORR occurs on the material. If n is somewhere between 2 and 4, both reactions occur on the material.

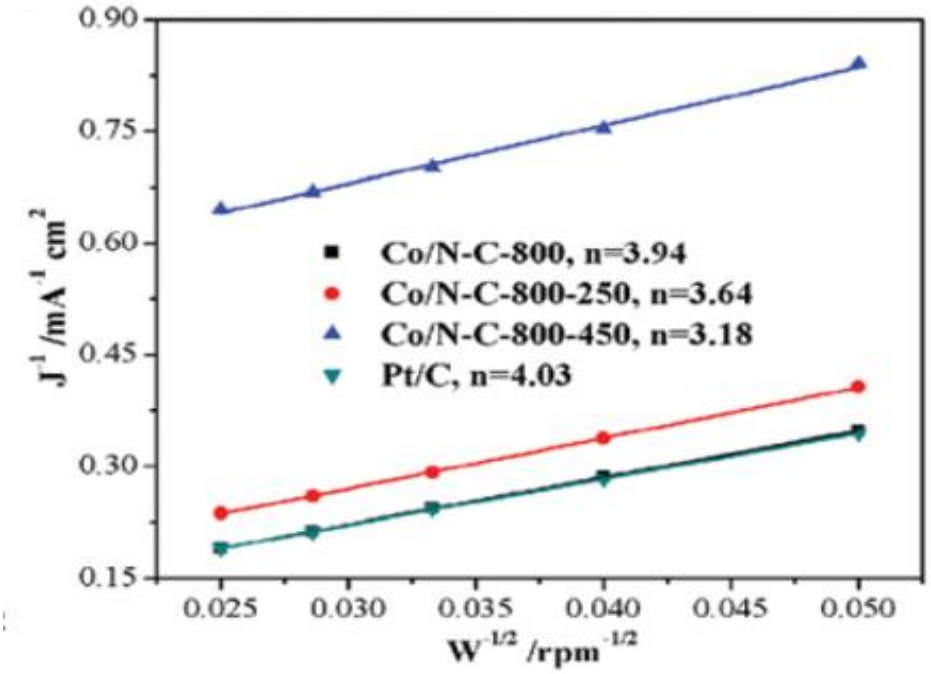

Figure 10. K-V plot of several Co-N/C electrodes and Pt/C electrode (from ref 29).

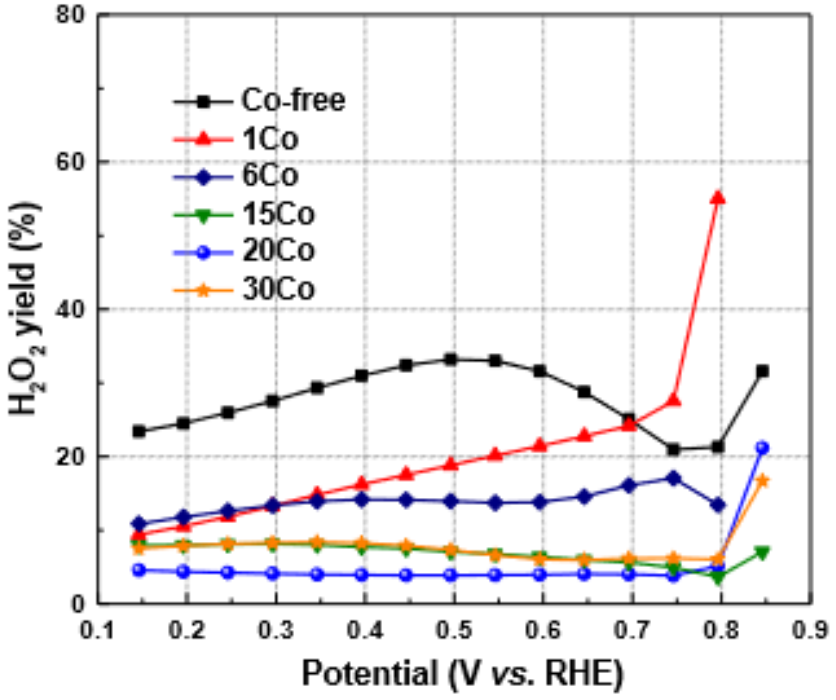

Figure 11. H_2O_2 yield on Co-N/C materials with various loadings(from ref 30).

A previous experimental research calculated n for their Co-N/C materials as well as Pt/C[29]. According to their result, the number of electron transferred for Pt/C is almost 4, suggesting its supreme selectivity. The same number for Co-N/C materials varies from 3 to 4, indicating both $2e^-$ ORR and $4e^-$ ORR occur on the material. Another research showed the selectivity of Co-N/C materials by measuring the H_2O_2 yield during the test[30]. The low H2O2 yield also suggests both $2e^-$ ORR and $4e^-$ ORR occur on the material.

While the experimental methods focus on the physical and electrochemical properties of the heat-treated mixture, the theoretical methods supported by density functional theory (DFT) are introduced to investigate and predict the atomic structures of the active sites as well as the reaction mechanism of ORR for non-precious TM-N/C materials. The computational study is mainly conducted through calculating the relative energy levels of all reaction species (such as *O, *OH, *OOH, etc for ORR) and predicting the electrochemical properties by analyzing the energy changes along the reaction coordinate.

A previous computational research assumed CoN4 cluster as the active site on Co-N/C materials[18]. By calculating the adsorption energy and plotting the free energy landscape, the result exhibited that the active energy of $4e^-$ ORR was 1.11eV. Such high active energy makes the reaction hardly happen. On the contrary, the $2e^-$ ORR analyze shows a high activity. The prediction of CoN4 cluster showed that only $2e^-$ ORR occurs on Co-N/C materials.

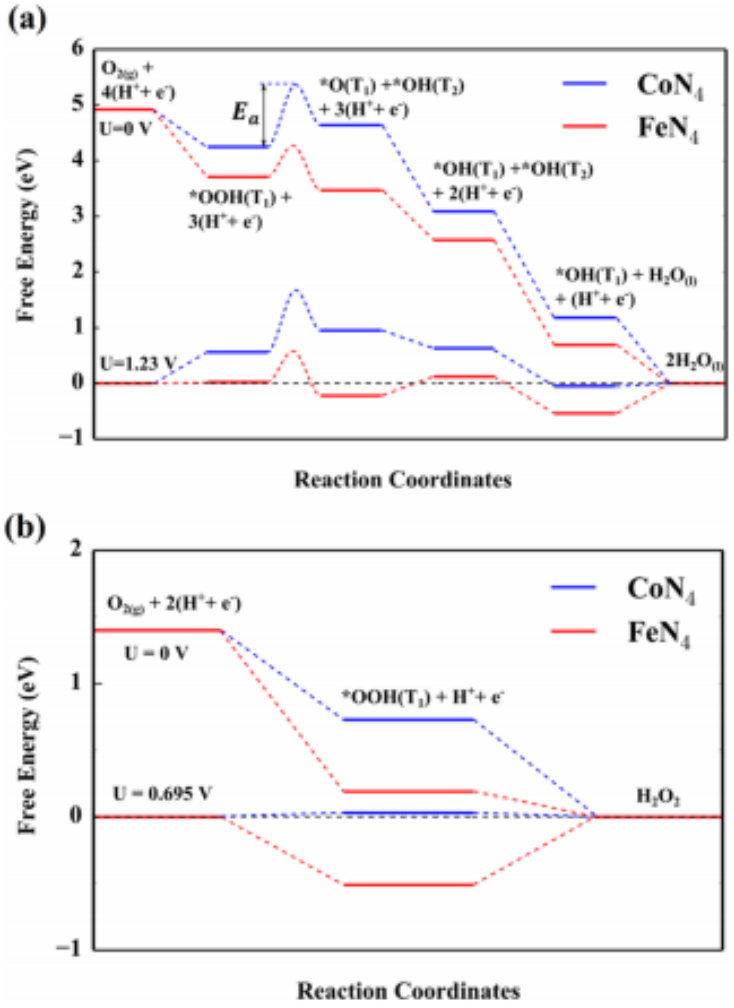

Figure 12. Free energy diagram for (a) $4e^-$ pathway and (b) $2e^-$ pathway (from ref 18).

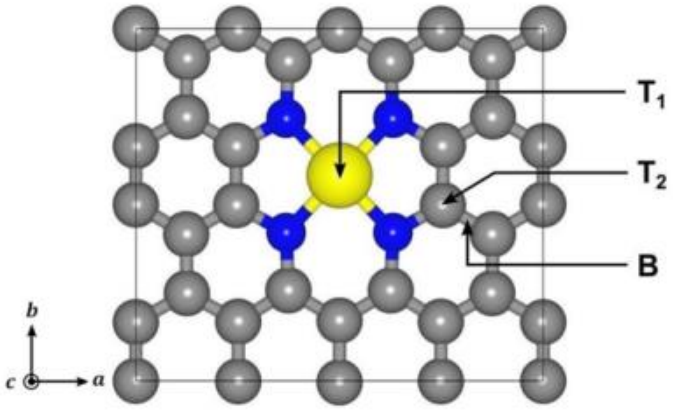

Figure 13. Atomic model of CoN_4 cluster. Grey, blue and yellow balls represent carbon, nitrogen and iron atoms, respectively (from ref 18).

1.3 HYPOTHESIS

For the same reaction of ORR occurring on Co-N/C materials, experimental study and computational study gave out the different results. The experimental result showed both $2e^-$ ORR and $4e^-$ ORR occur on the material, while the computational result suggested only $2e^-$ ORR happened. Yet the computational study only predicted the property of CoN_4 cluster, which did not match with the experimental result. In this case, there must be some other clusters on the material that serves as the active site of ORR, such as CoN_2, CoN_3 or CoN_5.

2.0 METHODS

The investigation of the mechanisms of ORR elemental reactions and competing reactions is conducted energetically. Free energy diagrams are plotted to visualize the reaction trends (such as Figure 14). A reaction is more thermodynamically favorable with a relatively low active energy and a relatively low value of enthalpy change.

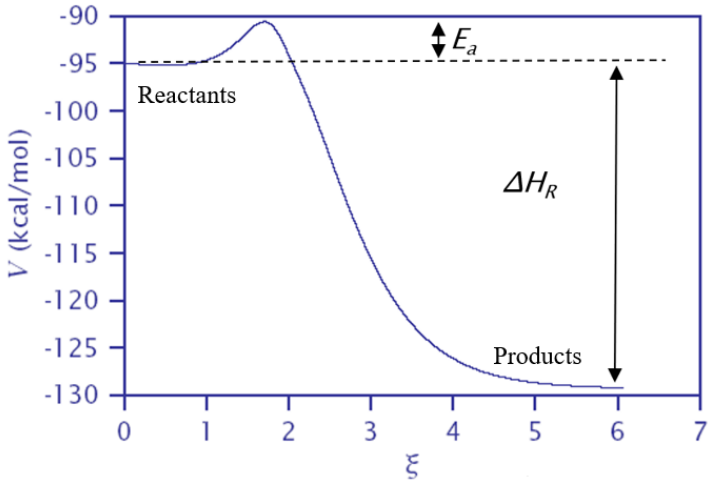

Figure 14. Energy diagram of a simple chemical reaction.

A similar method is employed to study two competing reactions (such as O-OH reduction). Containing the same elemental components, the products of the two reactions can transfer to each other. Therefore, a similar diagram can be plotted for the reversible reaction. By

comparing the products free energy of the two reactions, the one with lower products free energy is more thermodynamically feasible.

In conclusion, the ORR on the electrocatalyst surface is studied energetically, all relative energy is calculated by DFT method.

2.1 DENSITY FUNCTIONAL THEORY

Using the Vienna Ab-Initio Simulation Package (VASP) code[31,32], the DFT method solves the Schrodinger equation approximately[33]:

$$\hat{H}\varphi = E\varphi \tag{1}$$

For a system containing N electrons and K nuclei, the Hamiltonian $\hat{H}$ in Eq. (1) could be rewritten as:

$$\hat{H} = \hat{K} + \hat{P}_{e-e} + \hat{P}_{e-n} \tag{2}$$

$$\hat{K} = -\sum_{i=1}^{N} \frac{\hbar}{2m} \nabla_i^2 \tag{3}$$

$$\hat{P}_{e-e} = -\frac{1}{2}\frac{1}{4\pi\varepsilon_i}\sum_{i\neq j}^{N}\sum_{i\neq j}^{N}\frac{e^2}{|\vec{r_i} - \vec{r_j}|} \tag{4}$$

$$\hat{P}_{e-n} = -\frac{1}{4\pi\varepsilon_i}\sum_{i=1}^{N}\sum_{i=1}^{K}\frac{E_n e^2}{|\vec{r_i} - \vec{R_J}|} \tag{5}$$

Where $\hat{K}$ represents the kinetic energy of the system, $\hat{P}_{e-e}$ is the potential energy between electrons, $\hat{P}_{e-e}$ is the potential energy between electrons and nuclei. This is a many-body problem, especially the $\hat{P}_{e-e}$ term, containing all interactions between electrons. For a system

with dozens or hundreds of electrons, the calculation of the $\hat{P}_{e-e}$ term would be far too complex. Hence an assumption is made that the interaction between electrons equals to the effect of one electron on the average electron density of all the other electrons, to reduce the many-body problem to one-body problem, meanwhile introducing correlation error and self-interaction error. Two other assumptions are also made in DFT method that the ground state energy from Schrodinger equation is a unique function of the ground state electron density: E=E(n(r)), and the electron density that minimizes the energy of the overall function is the electron density corresponding to the full solution of the Schrodinger equation.

For each electron in the system, the one-body problem is described by Kohn-Sham equation[34]:

$$\left[-\frac{\hbar}{2m}\nabla^2 + V_r(\vec{r}) + V_H(\vec{r}) + V_{XC}(\vec{r})\right]\varphi(\vec{r}) = \varepsilon_i\varphi(\vec{r}) \tag{6}$$

Where $-\frac{\hbar}{2m}\nabla^2$ is the kenetic energy of the system, $V_r(\vec{r})$ is the electron-nuclei interaction, $V_{XC}(\vec{r})$ is the exchange correlation function, in this calculation, it is decribed within the framework of feneralized gradient approximation (GGA) of revised Perdew-Burke-Ernzerhof functionals (RPBE)[35], $V_H(\vec{r})$ is simplified electron-electron interaction called Hatree potential, calculated by:

$$V_H(\vec{r}) = e^2\int\frac{n(r')}{|r-r'|}dr^3 \tag{7}$$

The relative energy is calculated through a self-consistent approach. The initial electron density is assumed to obtain a wave function using Kohn-Sham equation, and subsequently result in a revised electron density. The calculation would stop when the two densities are close enough, otherwise the electron density would be updated and repeat the previous step.

In VASP calculation, pseudopotential, generated by projector augmented wave (PAW)[36,37], was employed with the assumption that the core electrons are relatively inactive and can be consider frozen. The wave functions were described using a plane wave basis set that can be adjusted by

kinetic energy cutoff of 400eV. The Brillouin zone was sampled with 4×4×1 k-point grid which is generated by Monkhorst-pack[38]. The atomic positions were optimized until the forces were below 0.01eV/Å. All the calculations were conducted in spin unrestricted manner.

2.2 CLIMBING IMAGE NUDGED ELASTIC BAND METHODS

The transition states and the active energy was obtained through the climbing image nudged elastic band (Cl-NEB) method, in which a string of images is introduced to describe a reaction pathway. The calculation starts with an initial assumed pathway connecting the initial and final states. The images are connected by spring forces and are relaxed by force projections to the minimum energy path (MEP).

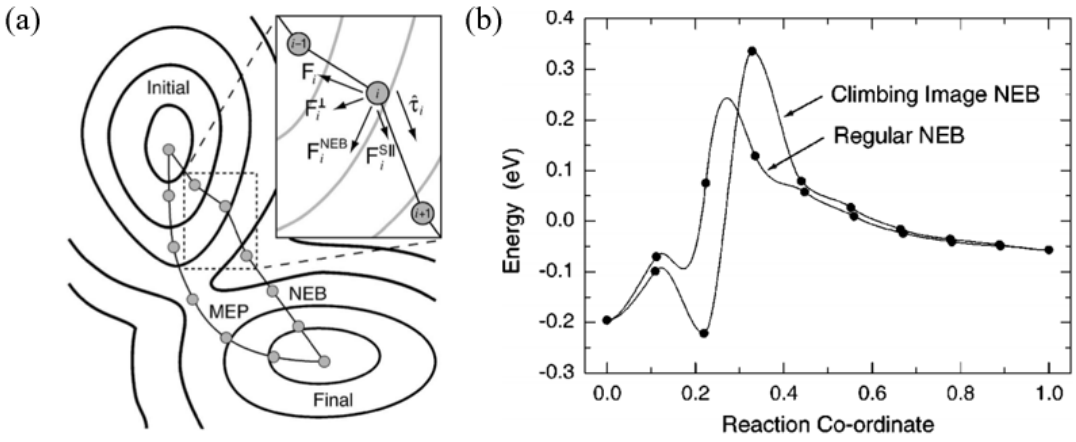

Figure 15. (a) The relaxation of images[39]. (b) The DFT calculation for CH_4 dissociation on Pt(111) surface[40].

In Figure 15(a), the NEB force on image i consists of a vertical component $F_i^{\perp}$ representing the potential gradient perpendicular to the band, and a horizontal component F_i^{SII}

which is the spring force parallel to the band. The saddle point is the image corresponding to transition state which is particularly important to the activate energy calculation for Arrhenius rate. Because of spring forces, the saddle point may lie between two of the images. In regular NEB calculation, the saddle point is obtained roughly and efficiently through a 'min-mode' following saddle point search from the highest energy state to find the transition state[41]. Another method to reach the saddle point is to let the highest energy image climb towards the high energy direction along the band until is takes no spring force (shown in Figure 15(b)). All images are relaxed until the all the force components are less than 0.05 eV/Å. The saddle points are further confirmed first order by vibrational analysis.

2.3 EFFECT OF ELECTRODE POTENTIAL

Due to the proton transfer between phases, the free energy of the electrocatalyst system is significantly influenced by electrode potential. To introduce the overpotential effect to this ORR study, which is out of VASP`s ability, a reference potential is set to be that of the standard hydrogen electrode (SHE) [22]. The initial reaction could be described as:

$$*P* + e^- + H^+ \rightarrow *PH \quad E=E_{ini} \tag{8}$$

The reaction on SHE could be shown as:

$$1/2H_2 \rightarrow H^+ + e^- \qquad E=eU \text{ (E=0 when U=0)} \tag{9}$$

With the condition of pH=0, P_{H2} =1bar and T=298K.By adding Eq. (8) with Eq. (9):

$$*P + 1/2H_2 \rightarrow *PH \quad E=E_{ini} + eU \tag{10}$$

The relative free energy of the system is calculated by:

$$\Delta G = \Delta E + \Delta ZPE - T\Delta S, \qquad . \tag{11}$$

Where is the difference of the system relative energy to the reactant relative energy, ΔE is the formation energy of the system, -TΔS is entropy correction term, n represents the number of free proton and U represents electrode potential. All the calculations were conducted with the assumption that pH=0, P_{H2} =1bar and T=298K.

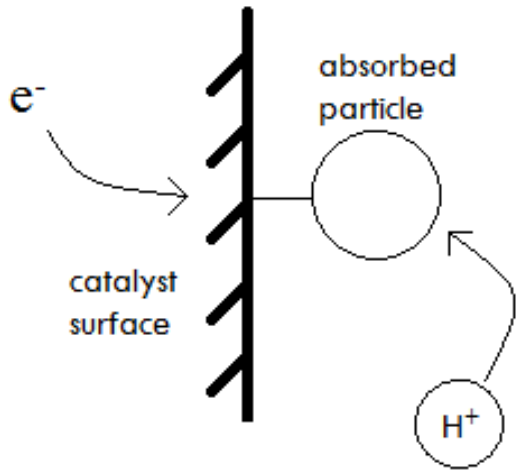

Figure 16. Electron transfer between two phases.

3.0 RESULTS AND DISSCUSION

Since the catalytic activity was first found for ORR on TM-N/C materials in 1964, lots of efforts have been made to study the reaction[11]. though the progress was huge, the true nature of this electrocatalyst is still not fully understood. It is reported that the transition metals like Fe and Co, combined with nitrogen atoms embedded in carbon base is responsible to the ORR catalytic activity. This TM-N_x cluster was observed in a recent microscope ORR study of a Fe and nitrogen doped graphene-carbon nanotube complex[17].

3.1 MODELS AND ADSORPTION ENERGIES

The active sites for ORR in TM-N/C material were often suggested to be planar TM-N_x clusters. The possibility of TM-N_x clusters act as ORR catalyst was further examined by theoretical study using DFT calculations. Though those researches claimed that among all the possible planar TM-N_x sites, the TM-N_4 cluster has the lowest formation energy[24], the other TM-N_x sites also exhibit fine adsorption of reactant O_2 and attract the H_2O weakly than the solvation stabilization energy of bulk water so that the products could easily detach from the surface. Therefore, the other planar TM-N_x sites (TM=Co, x=2,3,5, also 4 as reference) embedded in graphene are adopt in this DFT study the active sites of pyrolyzed Co/N/C materials.

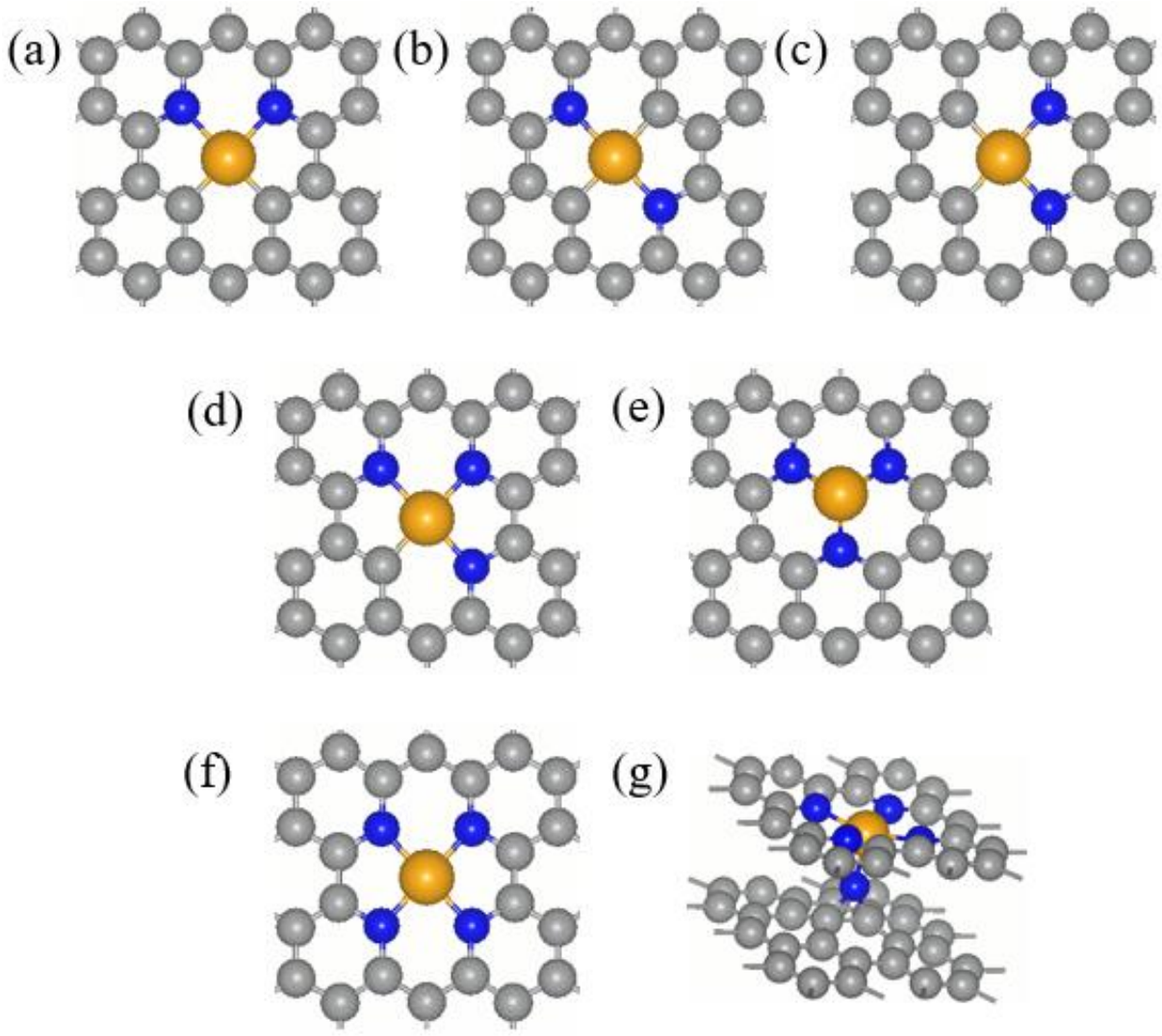

Figure 17. All adopted models of Co-N_x clusters. (a) CoN_2C_2(I), (b) CoN_2C_2(II), (c) CoN_2C_2(III), (d) CoN_3C, (e) CoN_3, (f) CoN_4 and (g) CoN_5.

In the figure, the yellow, blue and grey balls represent Co, N and C atoms, respectively. There are seven sties adopt in this study. The upper panel represent the Co-N_2 clusters (CoN_2C_2(I), CoN_2C_2(II) and CoN_2C_2(III)), The middle panel stand for Co-N_3 clusters (CoN_3C and CoN_3), the last two show the structure of Co-N_4 and Co-N_5 clusters respectively (CoN_4 and CoN_5). All clusters are modelled in a 32-atom (66-atom for site 5-1) graphene super cell. The lattice parameters are a=9.84Å and b=8.52Å. Periodic boundary are employed in all three dimensions. The periodic images of the graphene layers are separated by a 14Å (17 Å for site 5-1) vacuum in the vertical direction of the layer to reduce the interaction of neighbor images. In the graphene unit cells, the central two carbon atoms are replaced by the Co atom and the four surrounding carbon atoms are substitute with x (x=2,3,4) nitrogen atoms and 4-x carbon atoms. In the CoN_3 cluster, the three N atoms are slightly above the graphene layer to ensure the C-N bonds are stable and the Co atom is even further from the graphene layer for the same reason. The upper layer of CoN_5 cluster is the same with site 4-1, while an additional nitrogen atom is placed between the two graphene layers.

Using the DFT method, the adsorption energies of some possible species of ORR on Co-N_x active sites are obtained by calculating the energy difference of the adsorbed system and the separated Co-N_x slabs and ORR species in gas phase. Hence the lower adsorption energy the specie has, the stronger the adsorption is.

Table 1. Calculated adsorption energies (eV) of ORR species on Co-N_x clusters. Strong ORR species adsorptions are marked in red.

M: metal top site. C: carbon top site. B: bridge site.

ORR species	**Adsorption sites**	**CoN_2C_2 (I)**	**CoN_2C_2 (II)**	**CoN_2C_2 (III)**	**CoN_3C**	**CoN_3**	**CoN_4**	**CoN_5**
H	M	-2.53	-2.44	-2.61	-2.38	-	-2.27	-2.01
H	C	-2.55	-2.96	-2.79	-2.56			
O	M	-3.93	-4.01	-3.97	-3.79	-5.16	-3.19	-2.60
O	B	-4.55	-5.07	-4.95	-4.52			
OH	M	-2.93	-2.86	-2.81	-2.70	-4.13	-2.42	-2.20
OH	B	-1.89	-2.37	-2.24	-			
O_2	M	-0.91	-1.11	-0.85	-0.72	-2.49	-0.65	-0.33
H_2O	M	-0.19	-0.19	-0.20	-0.03	-0.31	-0.04	-0.01
OOH	M	-1.60	-1.75	-1.53	-1.50	-2.73	-1.23	-1.10

Table 1 gives the result of adsorption energies. The M adsorption site is the top site of the central metal (Co in this case), C represents the carbon top site and B is the bridge site located somewhere above the layer and between the metal atom and its neighbor carbon atom. In this DFT calculation, the O_2 species is predicted to be quite favorably adsorbed on the central Co atom. The given adsorption energy of O_2 on this TM/N/C material could match with that of Pt catalysts, which is about -0.69eV on Pt(111)[42] surface and -1.10eV on Pt(111)[43] surface. The result suggests that the CoN_x sites are energetically favorable for ORR initiation. Besides, the adsorption of the ORR product H_2O is relatively weak with the adsorption energy less than 0.3eV. In comparison with the solvation stabilization energy of bulk water at 0.4eV, the H_2O species could be released from the catalyst surface spontaneously and move into electrolyte.

Comparing to the adsorption energies on CoN_4 cluster, the adsorption energies of all ORR species for CoN_5 cluster is a little higher, indicating the adsorption of ORR species on CoN_5 cluster is less energetically favorable than that of CoN_4 cluster. Similarly, the adsorption energies of all species for CoN_3C and CoN_3 clusters are lower than that of CoN_4 cluster. As the number of N atoms decreases, the adsorptions on CoN_2C_2(I), CoN_2C_2(II) and CoN_2C_2(II) clusters are even much stronger. The result implies that the CoN_x sites with less N atoms are more favorable to initiate ORR.

It is noticed that there exists a bridge site lies above the middle position between the central Co atom and the surrounding C atom. With the absence of the adsorption resisting N atoms, the bridge site could only be observed on CoN_xC_{4-x} (x=2,3) sites. An example of bridge site adsorption is demonstrated in Figure 18.

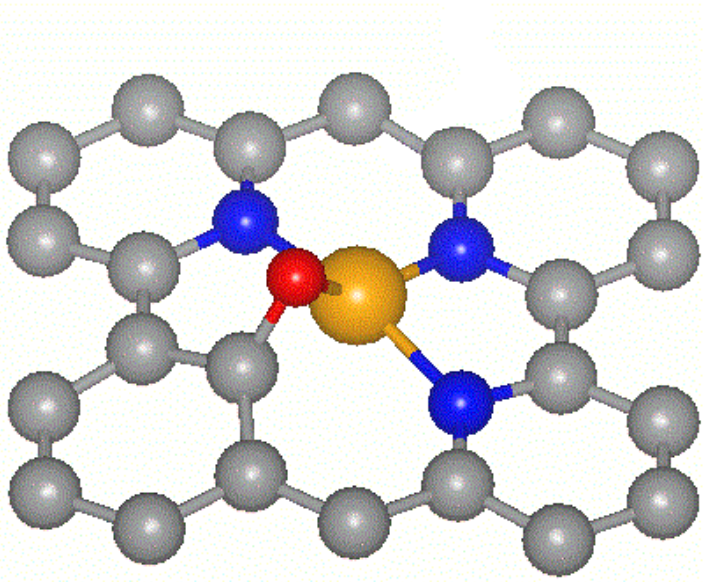

Figure 18. The bridge site adsorption of O on CoN_3C.

Table 2. Calculated adsorption energies (eV) on bridge sites.

M: metal top site. B: bridge site.

ORR species	**Adsorption sites**	**CoN_2C_2 (I)**	**CoN_2C_2 (II)**	**CoN_2C_2 (III)**	**CoN_3C**
O	M	-3.93	-4.01	-3.97	-3.79
O	B	-4.55	-5.07	-4.95	-4.52
OH	M	-2.93	-2.86	-2.81	-2.70
OH	B	-1.89	-2.37	-2.24	-

Though the adsorption breaks the Co-C bond with the Co-N distance larger than 2.3 Å, the adsorption system is quite thermodynamically stable supported by Table 1. This strong adsorption that effects the OOH dissociation will be in the later sector.

By comparing the adsorption energies on metal top site and bridge site, it is obviously obtained that the O adsorptions on bridge site are much stronger than metal top site, while the OH adsorptions on bridge site are weaker.

As a result, a conclusion is summarized that all CoN_x clusters show a high possibility to act as active site for ORR and the N atoms on in CoN_x clusters weaken the adsorption of all ORR species on the active sites. Though the CoN_x clusters seem to attract all ORR species stronger, the adsorptions are so strong that it may prevent some reactions from happening. Which is further confirmed in free energy calculation.

The extreme strong ORR species adsorption (especially for the adsorbed O) obtained in previous work suggests that the adsorbed O systems on CoN_x clusters are quit thermodynamically stable. Using a computational method developed earlier[44], the free energy level of the system is later calculated to investigate the last two steps of the ORR $4e^-$-pathway. The result of free energy calculation implies that there exist more than one energy barriers along the reaction path on CoN_2C_2(II), CoN_2C_2(III) and CoN_3 clusters, resulting the catalyst poisoned at the corresponding reaction coordinate. In this regard, CoN_2C_2(II), CoN_2C_2(III) and CoN_3 are considered not qualified as ORR active sites. Therefore, theses three clusters are not discussed in further study.

The strong adsorption of O on bridge site also leads to another idea that the thermodynamically stable cluster with adsorbed O might still be active for ORR. In this regard, 4 other clusters are set to prove this idea.

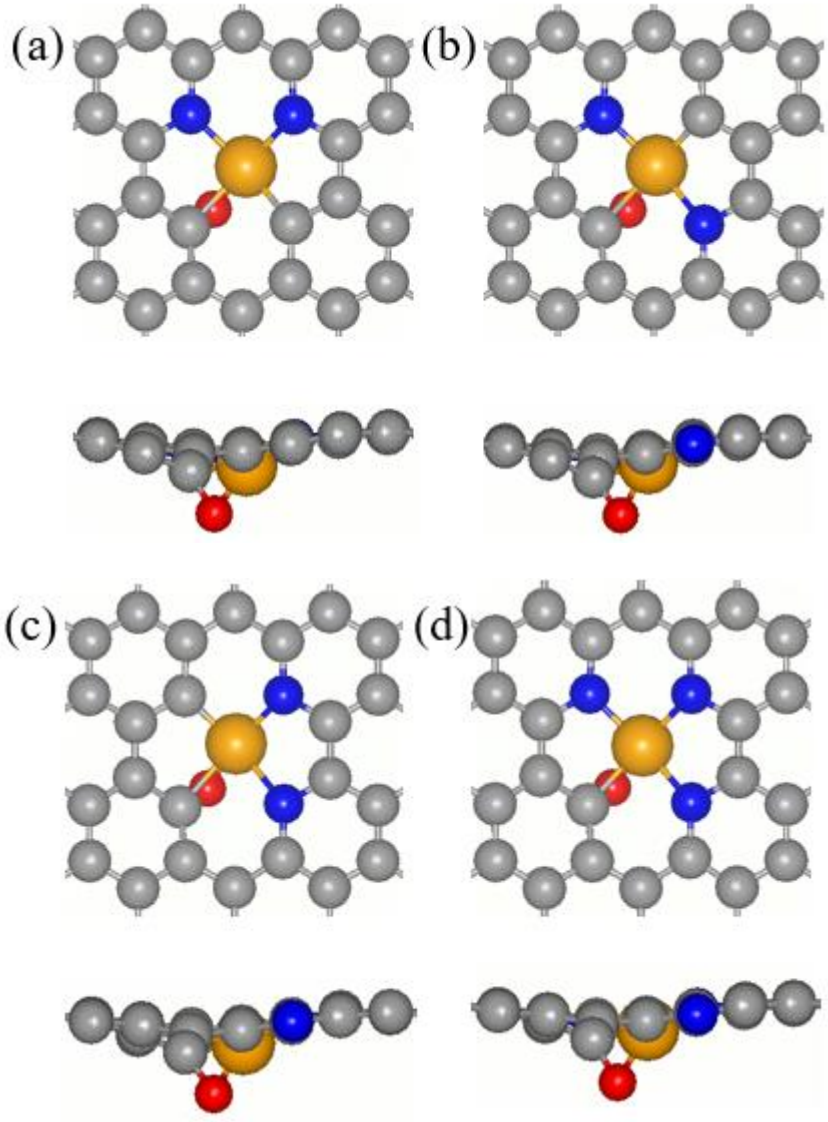

Figure 19. All adopted models of Co-N_xO clusters.

(a) CoN_2C_2O(I) (b) CoN_2C_2O(II) (c) CoN_2C_2O(III) (d) CoN_3CO

These four clusters are similar to CoN_2C_2(I), CoN_2C_2(II), CoN_2C_2(III) and CoN_3C clusters, the only difference is the addition O atom on bridge site. The calculated adsorption energies are demonstrated below:

Table 3. Calculated adsorption energies (eV) of ORR species on CoN_xO clusters. Strong or weak ORR species adsorptions are marked in red.

ORR species	**Adsorption sites**	**CoN_2C_2 (I)**	**CoN_2C_2 (II)**	**CoN_2C_2 (III)**	**CoN_3C**
H	M	-2.55	-2.38	-1.95	-1.92
H	C	-2.50	-2.59	-2.10	-1.61
O	M	-3.58	-3.69	-3.347	-3.54
O	B	-4.73	-4.68	-4.09	
OH	M	-1.72	-2.90	-2.55	-2.65
OH	B	-2.06	-2.26	-1.99	
O_2	M	-0.47	-0.77	-0.46	-0.45
H_2O	M	-0.12	-0.02	-0.06	-0.04
OOH	M	-1.32	-1.65	-1.08	-1.05

According to Table 3. The O adsorptions on bridge site of CoN_2C_2O(I) and CoN_2C_2O(II) clusters are still too strong. For the same reason, this two clusters are not discussed in further investigation. Besides, the OOH adsorption on CoN_3CO is relatively weak. Thus, this cluster is not included in further research. The OOH adsorption on CoN_2C_2O(III) is also relative weak, but the acceptable O adsorption strength keeps it remain in further discussion.

3.2 O_2 DISSOCIATION AND OOH DISSOCIATION

The reaction pathway of ORR on TM-N_4 was investigated to prefer the OOH dissociation in a previous sdudy[18]. It is reported that the O_2 dissociation requires an active energy of 1.96eV for Co-N_4 and 1.19eV for Fe-N_4 by obtaining the transition states of O_2 dissociation and saddle using the Cl-NEB method. It shows that the huge energy gap makes the O_2 dissociation too difficult to occur.

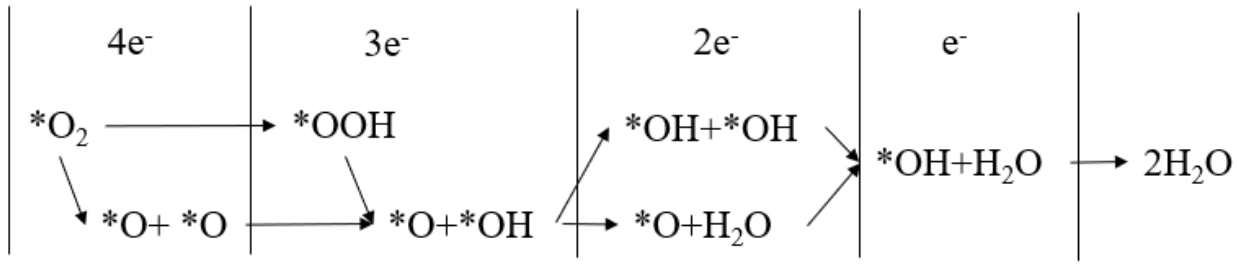

Figure 20. Possible routes of 4e- ORR

The appearance of bridge site adsorption dramatically lowers the free energy levels of O_2 products. This increase the possibility for O_2 dissociation to occur. In this regard, O_2 dissociation is investigated to discover the effect of bridge site to ORR.

According to Figure 22, due to the strong bridge site adsorption of O, the energy levels of the final state are lower than that of the initial state on CoN_2C_2(I) and CoN_3C cluster. Yet the transition state calculation indicates such conclusion doesn`t change the fact that O_2 dissociation requires huge amount of active energy. The active energies required by O_2 dissociation are 1.50eV and 1.10eV respectively. In Figure 21, there is no bridge adsorption on CoN_4 and CoN_5 clusters. As expected the energy levels of the products are much higher than that of reactants.

Active energy calculation is not necessary since the enthalpy changes of the reaction are both over 1.50eV. the active energies on these two clusters must be higher than that.

Compared to the active energy of 1.11eV for OOH dissociation on CoN_4 cluster in previous study, the O_2 dissociation is not energetically favorable on all clusters mentioned in this study.

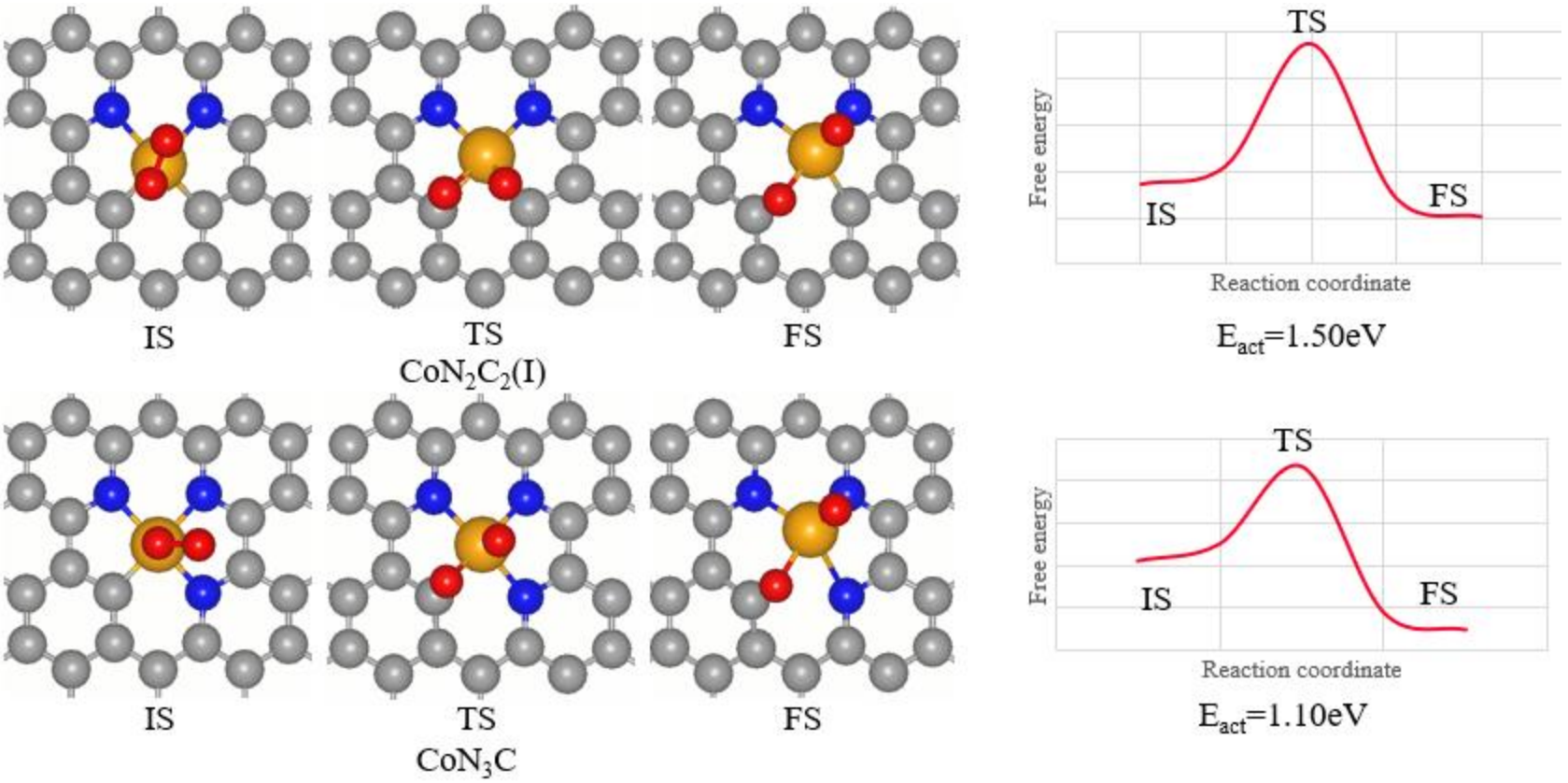

Figure 21. Atomic structures of the initial state (IS), the transition state (TS) and the final state (FS) as well as the free energy changes of O_2 dissociation on $CoN_2C_2(I)$ and CoN_3C clusters. Due to the bridge site adsorption, the free energy levels of the FS are lower than that of the IS.

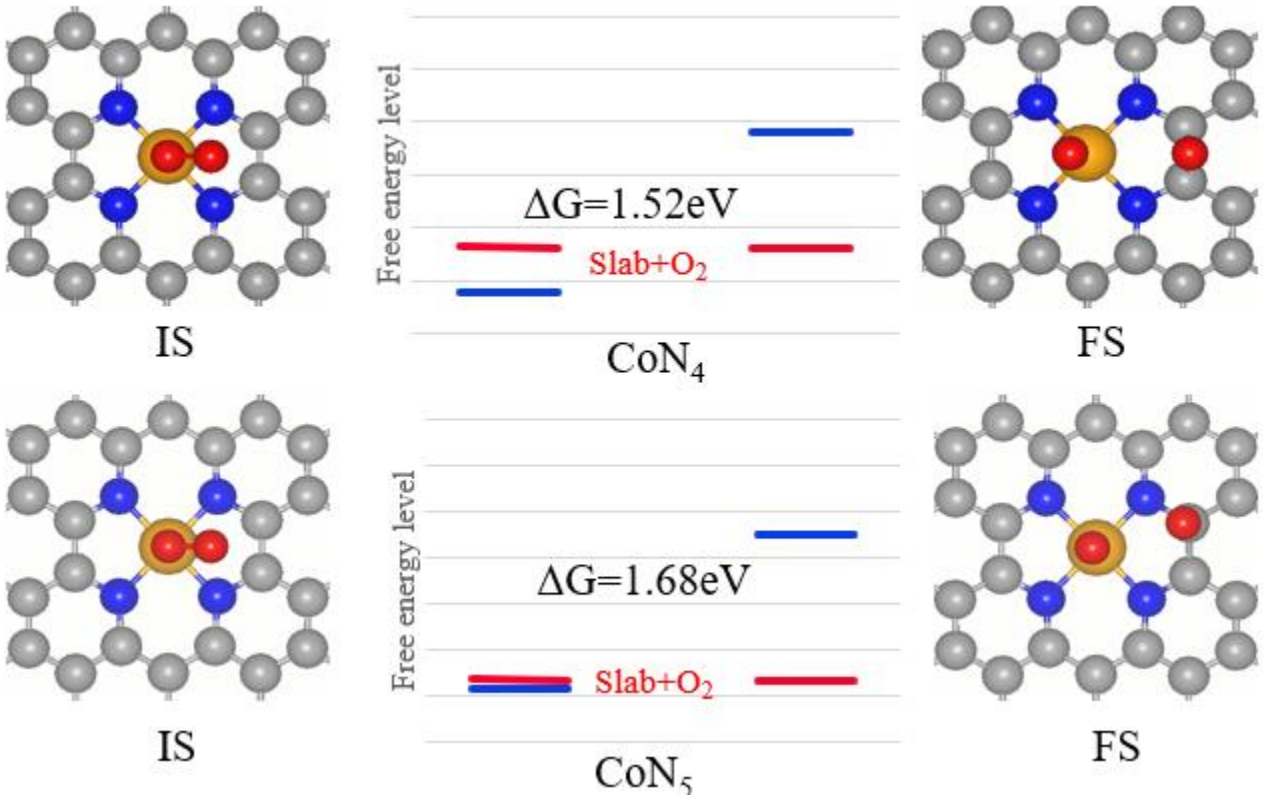

Figure 22. Atomic structures and Free energy levels of IS and FS of O_2 dissociation on CoN_4 and CoN_5 clusters. The active energies mus be higher than 1.50 eV.

In the previous sector, it is discussed that after the adsorption of the reactant O_2, the protonation of the adsorbed O_2 is the next step of ORR, forming the adsorbed OOH system. compared with the strong O-O bond in the adsorbed O_2 system, The O-O bond is weakened by the additional H atom, making the bond easier to break. Unless the reaction goes along the $2e^-$-pathway, the adsorbed OOH species would break the O-O bond for further reduction. As the dominating reaction in ORR with the highest active energy, the OOH dissociation is studied in detail trying to explain the mechanism of this elemental reaction. The initial state of OOH dissociation is the adsorbed OOH system, and the final state is the separated adsorbed O and adsorbed OH system. That transition state is obtained through Cl-NEB method and shall be found somewhere between them with a breaking O-O bond. The free energy difference of the initial state and that of the transition state is noted as the active energy of OOH dissociation, which is quite important in reaction analysis.

The whole mechanism is shown in Figure 13. In initial states of OOH dissociation on Co-N_x sites, the OOH species is adsorbed directly on the top of the central Co atom. As the reaction goes forward along the reaction coordinate, the distance of the two O atoms increases indicating the breaking of the O-O bond. In the reaction processes of CoN_2C_2(I) and CoN_3C clusters, the O atom closer to the graphene slab moves to the bridge site due to the strong bridge site adsorption of ORR species. At the same time, the other O atom moves toward to the central Co atom and finally linked on the central Co atom. For CoN_4 and CoN_5 clusters, the first O atom remains on the top site of the central Co atom, while the other O atom moves to the top site of the adjacent carbon atom. The calculated free energies of OOH dissociation on the four clusters are 0.78eV, 0.99eV, 1.20eV and 1.30eV respectively. It is obviously that the more nitrogen atoms the cluster contains, the higher the active energy OOH dissociation requires.

The OOH dissociation on CoN_2C_2O(III) cluster follows the same rule of CoN_2C_2(I) and CoN_3C clusters. Tough there are only 2 N atoms in the cluster, the OOH dissociation still requires an extremely high active energy of 1.50 eV. By analyzing the configuration of is transition state, the reason of the high active energy might come from the long distance between the Co atom and the outer O atom. The distance is 2.7 Å on CoN_2C_2O(III) while the same distance on CoN_2C_2(I) cluster is only 2.2 Å. The long distance weakens the catalytic effect of Co atom to the O-O bond breaking, thereby increases the active energy.

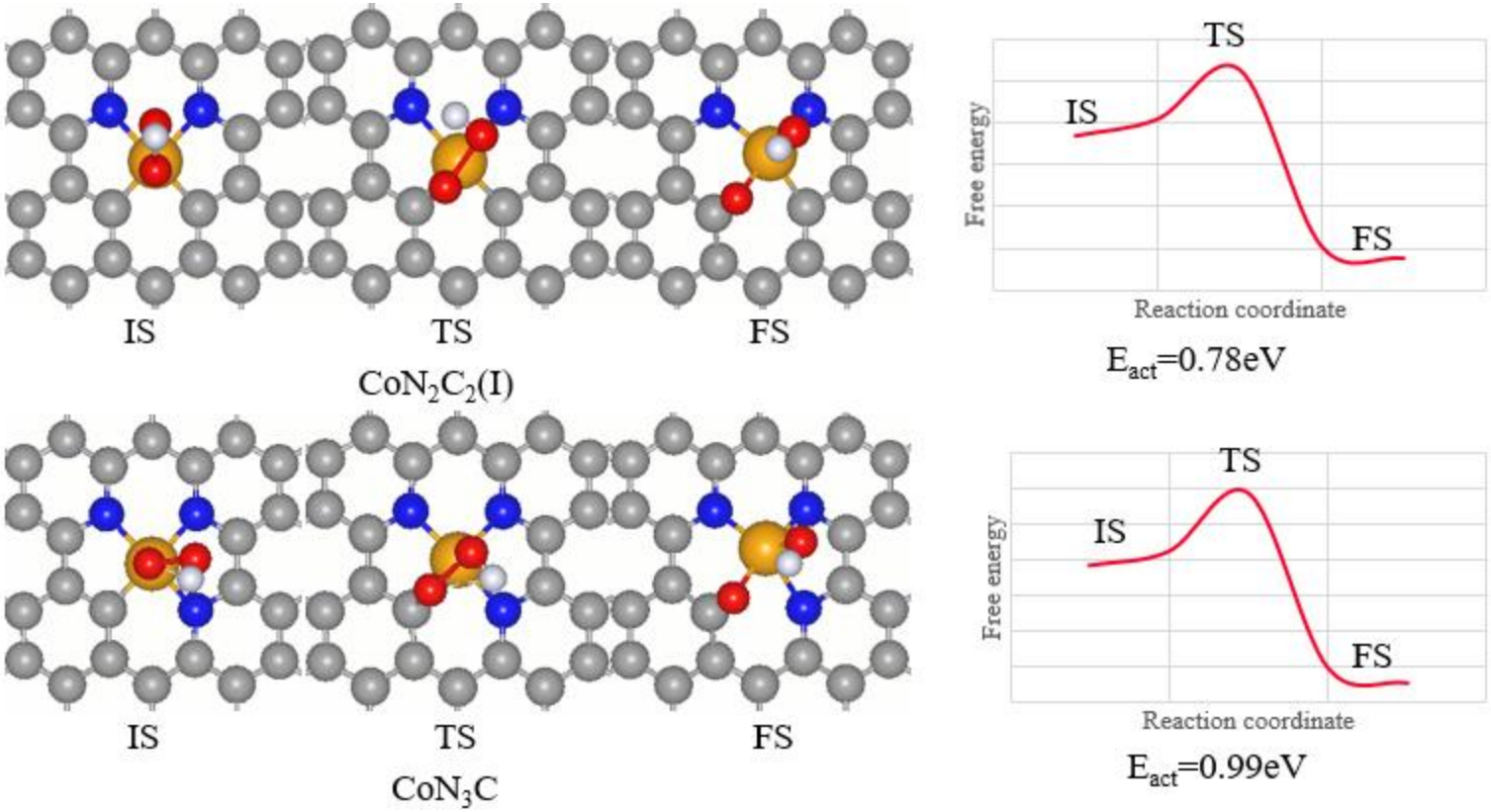

Figure 23. Atomic structures of IS, TS and FS as well as the free energy changes of OOH dissociation on $CoN_2C_2(I)$ and CoN_3C clusters.

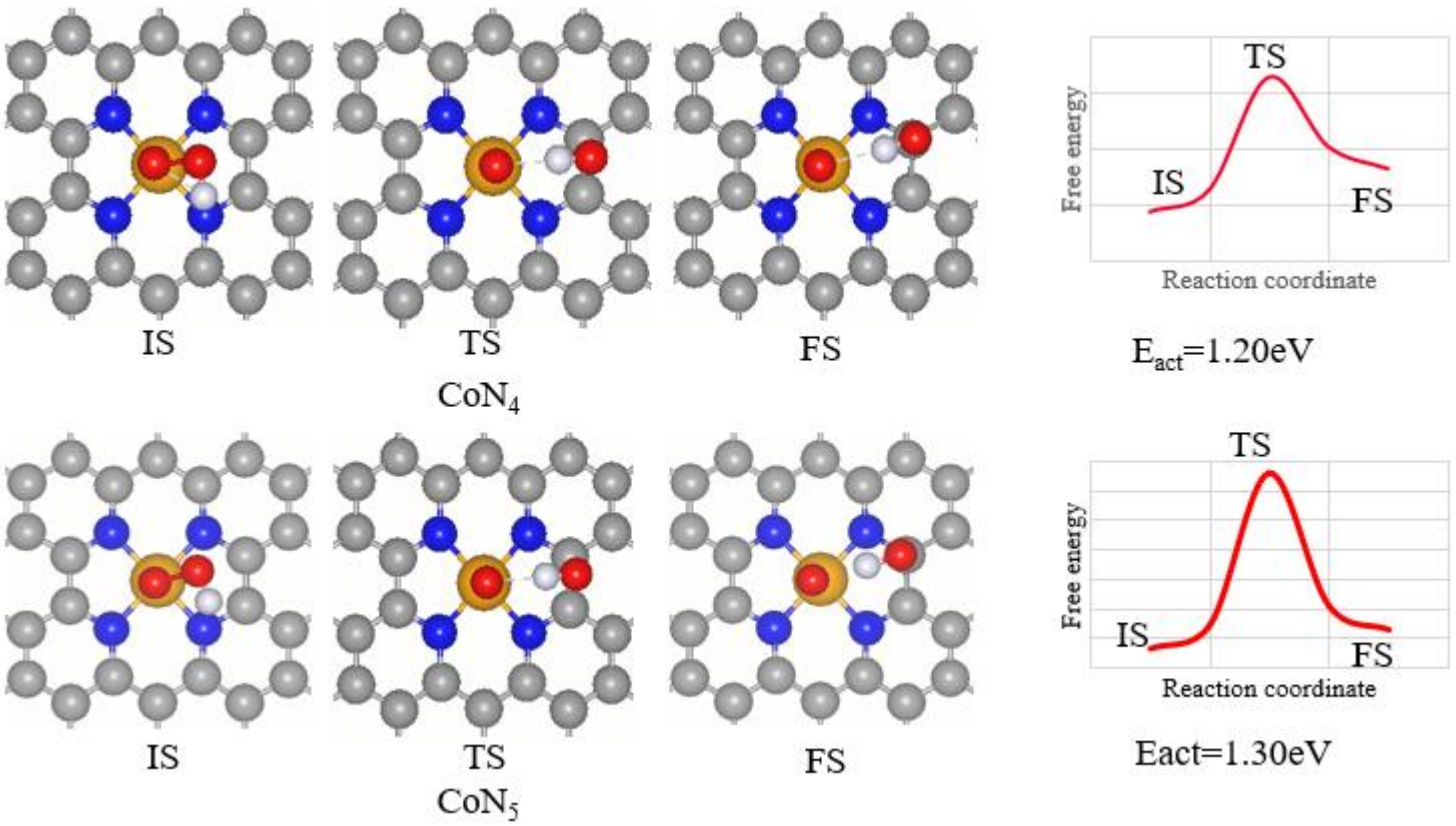

Figure 24. Atomic structures of IS, TS and FS as well as the free energy changes of OOH dissociation on CoN_4 and CoN_5 clusters.

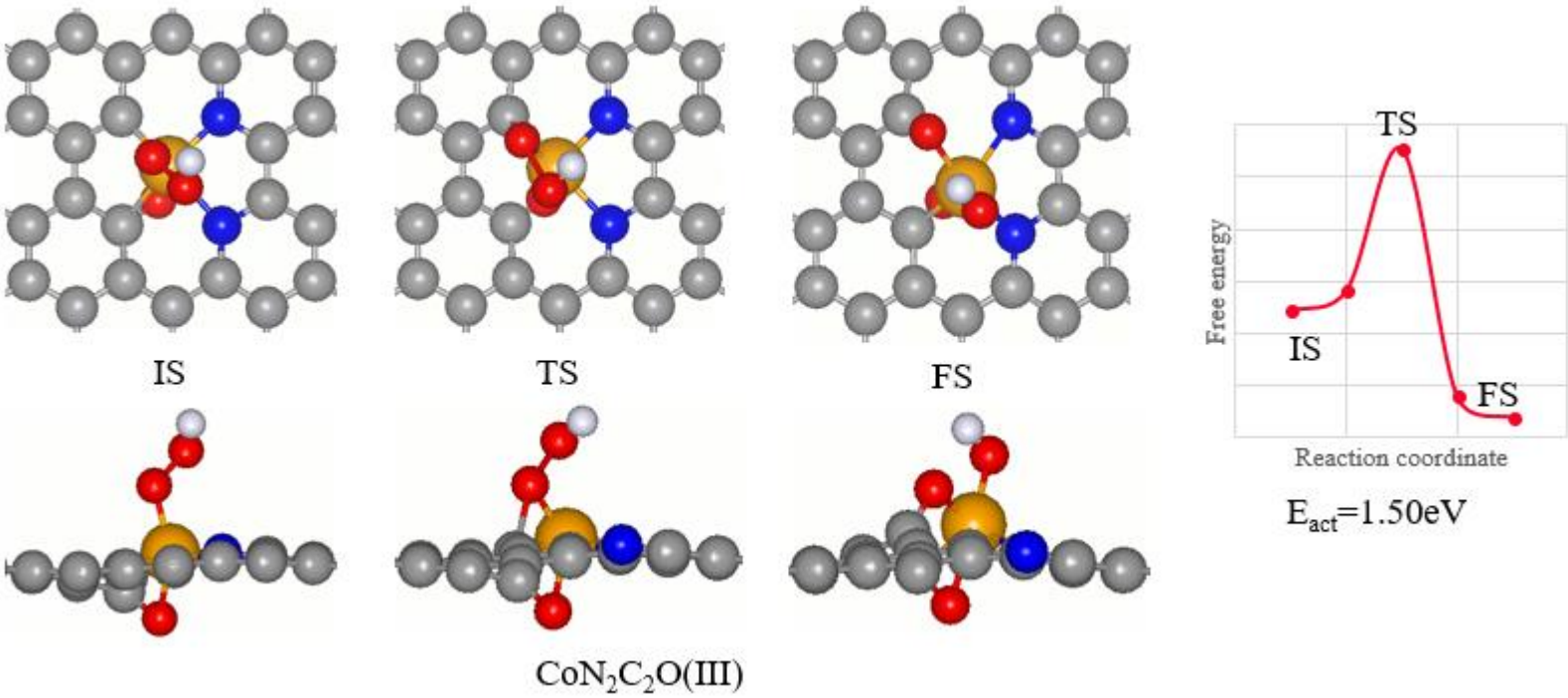

Figure 25. Atomic structures of IS, TS and FS as well as the free energy change of OOH dissociation on CoN_2C_2O(III) cluster.

It is noticed that the bridge site adsorption of O breaks the Co-C bond and force the central Co atom to move to the opposite direction. The movement is observed in the final states of ORR dissociation on CoN_2C_2(I) and CoN_3C clusters. To maintain the stability of the system, the distances of the central Co atom and the surrounding N atoms are ensured by the movement of the Co atom above the graphene layer.

Table 4. Energy barriers of O2 dissociation and OOH dissociation on CoN_2C_2(I), CoN_3C, CoN_4 and CoN_5 clusters

	CoN_2C_2(I)	CoN_3C	CoN_4	CoN_5
O2 dis.	E_{act}=1.50eV	E_{act}=1.10eV	E_{act}>ΔG=1.52eV	E_{act}>ΔG=1.68eV
OOH dis.	E_{act}=0.78eV	E_{act}=0.99eV	E_{act}=1.20eV	E_{act}=1.30eV

The transition states are further confirmed in frequency analysis to have one and only one imaginary frequency. The active energy is calculated to be 0.76eV, 0.95eV, 1.15eV and 0.93eV respectively. The result implies that the active energy of OOH dissociation on CoN_x sites rises with the increasing number of N atoms and falls at x=5. It seems that the active energy of OOH dissociation and the formation energy of CoN_x share a same relevance to the number of N atoms. However, this opinion is not confirmed yet.

The comparison of the energies required by O-O bond breaking shows that the OOH dissociations are much easier than O_2 dissociation on all clusters since the O-O bonds are weakened by the additional H atom. Thus, the 4e- ORR on all clusters would occur along the OOH dissociation path.

3.3 O-OH REDUCTION

The final state of the OOH dissociation is further reduced in O-OH reduction reaction. Distinguished by which oxygen atom is the next to be reduced, the O protonation and the OH protonation are the two possible pathways in this reduction reaction.

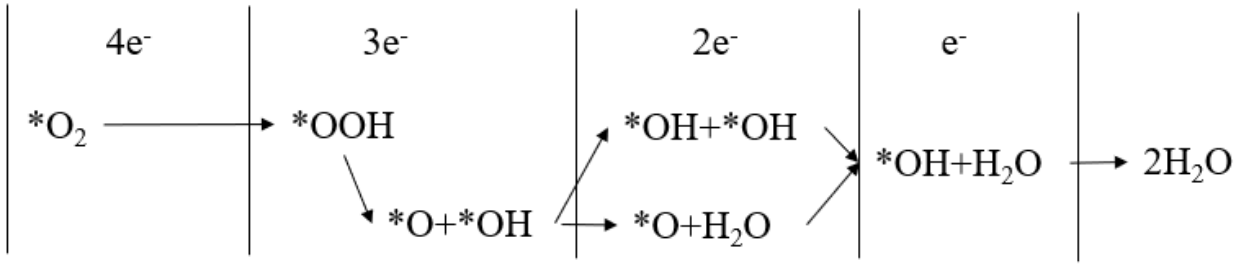

Figure 26. Possible routes of $4e^-$ ORR (after OOH dissociation).

In the OH protonation, the oxygen atom linked with a H atom is reduced, forming an adsorbed H_2O species. However, due to the weak adsorption of H_2O on Co-N_x sites, the H_2O molecule detaches from the graphene layer, yet weakly adsorbed on the surface. The adsorption energies of H_2O species in these cases are calculated to be less than the solvation stabilizing energy of bulk water of 0.2eV, which allows the H_2O molecules to be released into electrolyte. In the O protonation, the other oxygen is reduced, forming two adsorbed OH species.

Since O-OH reduction is not the dominant reaction in the whole 4e- ORR process, the choices of O-OH reduction pathway are simplified to the comparison of the enthalpy levels of the products. Besides, the two products contain exactly the same atoms, and can transform in to each other in certain circumstances. The reversible reaction can be written as :

$$^*OH + ^*OH \longleftrightarrow ^*O + H_2O$$

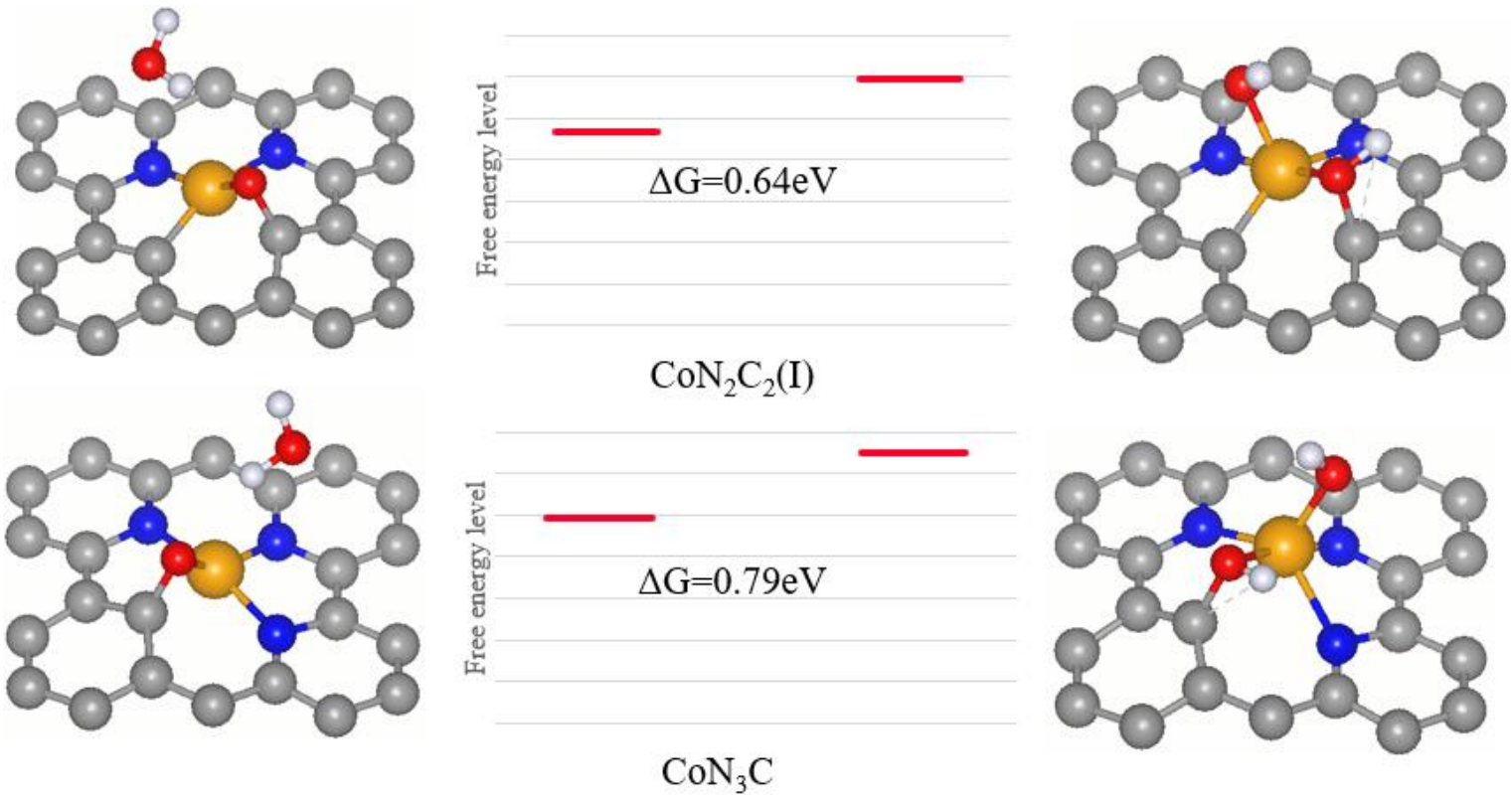

Figure 27. Atomic structures and free energy levels of *O+H_2O states and *OH+*OH states on CoN_2C_2(I) and CoN_3C clusters.

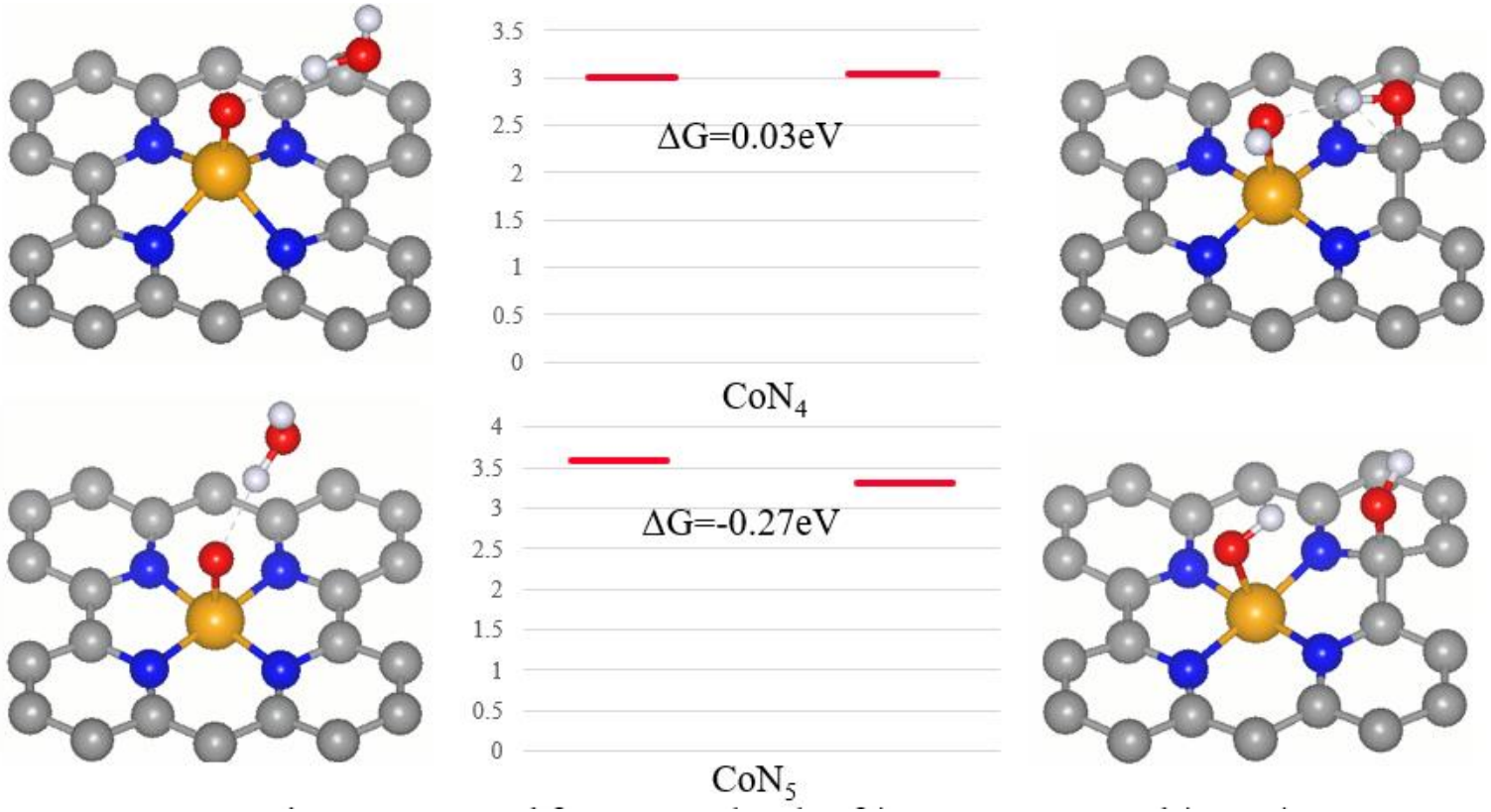

Figure 28. Atomic structures and free energy levels of *O+H_2O states and *OH+*OH states on CoN_4 and CoN_5 clusters.

The positive value of ΔG means the O-OH reduction prefers OH protonation. As shown in Figure 27 and 28, OH protonation is more thermodynamically feasible on CoN_2C_2(I) and CoN_3C clusters. O protonation was reported to be the O-OH reduction process on CoN_4 cluster by earlier studies and is quite favorable on CoN_5 cluster due to the negative value of ΔG.

The difference in O-OH reduction on CoN_x sites may also be explained by the strong bridge site adsorption. As shown in Table 1, the O adsorptions on the bridge site for CoN_2C_2(I) and CoN_3C clusters are much stronger than the OH adsorptions, especially the OH adsorption on the bridge site for CoN_3C is too weak to be found in DFT calculation. The result makes the bridge site adsorption of O atom more thermodynamically stable, thereby lowers the enthalpy level of the O-H2O system, which is the product of OH protonation.

Therefore, in this study, the OH protonation is calculated as O-OH reduction procedure on CoN_2C_2(I) and CoN_3C clusters, the O protonation is discussed for O-OH reduction on CoN_4 and CoN_5 clusters. The $4e^-$ ORR on CoN_2C_2O(III) cluster is assumed going along the O-H_2O pathway due to the existence of bridge site adsorption.

3.4 FREE ENERGY LANDSCAPES

The free energy evolutions of ORR pathway on Co-N_x sites are plotted in Figure 29 and 30 with an assumed temperature of 300K. The ORR pathway consists a sequence of O_2 protonation reaction, OOH dissociation reaction, O-OH reduction reaction and two O protonation reactions or OH protonation reactions. All species in those reactions are included in the plots.

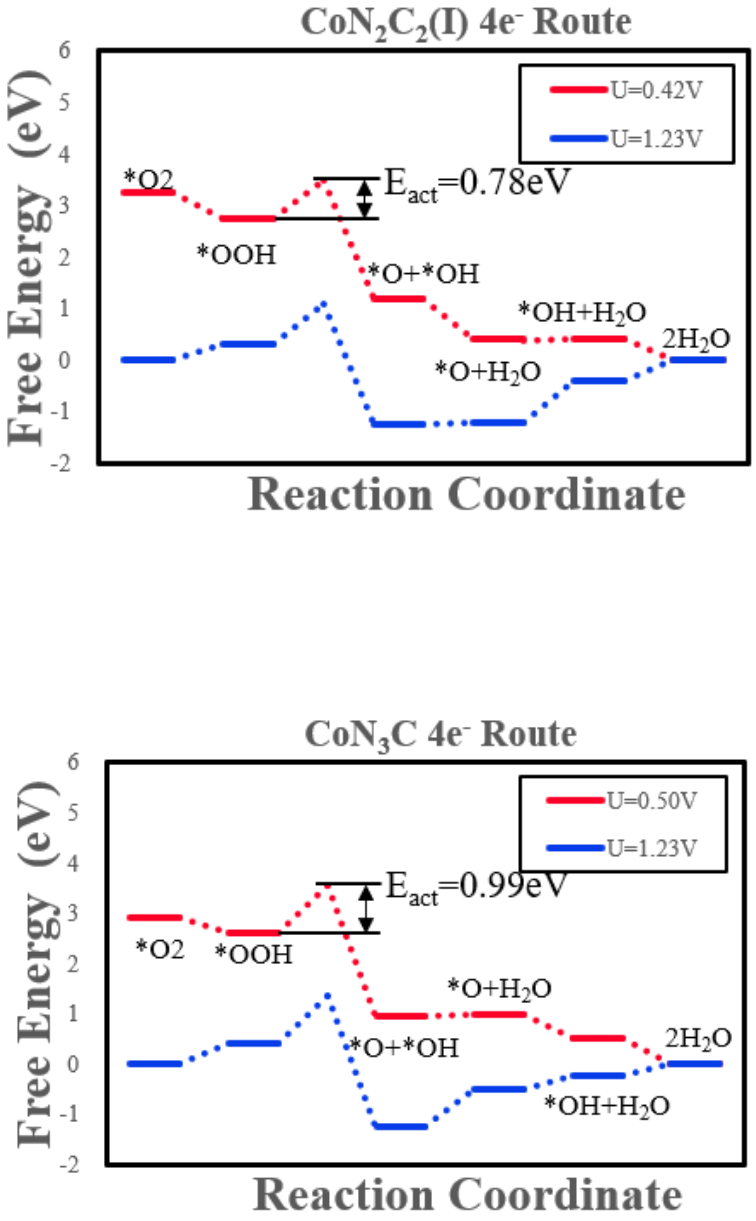

Figure 29. Free energy landscapes of 4e⁻ ORR on CoN_2C_2(I) and CoN_3C clusters**.**

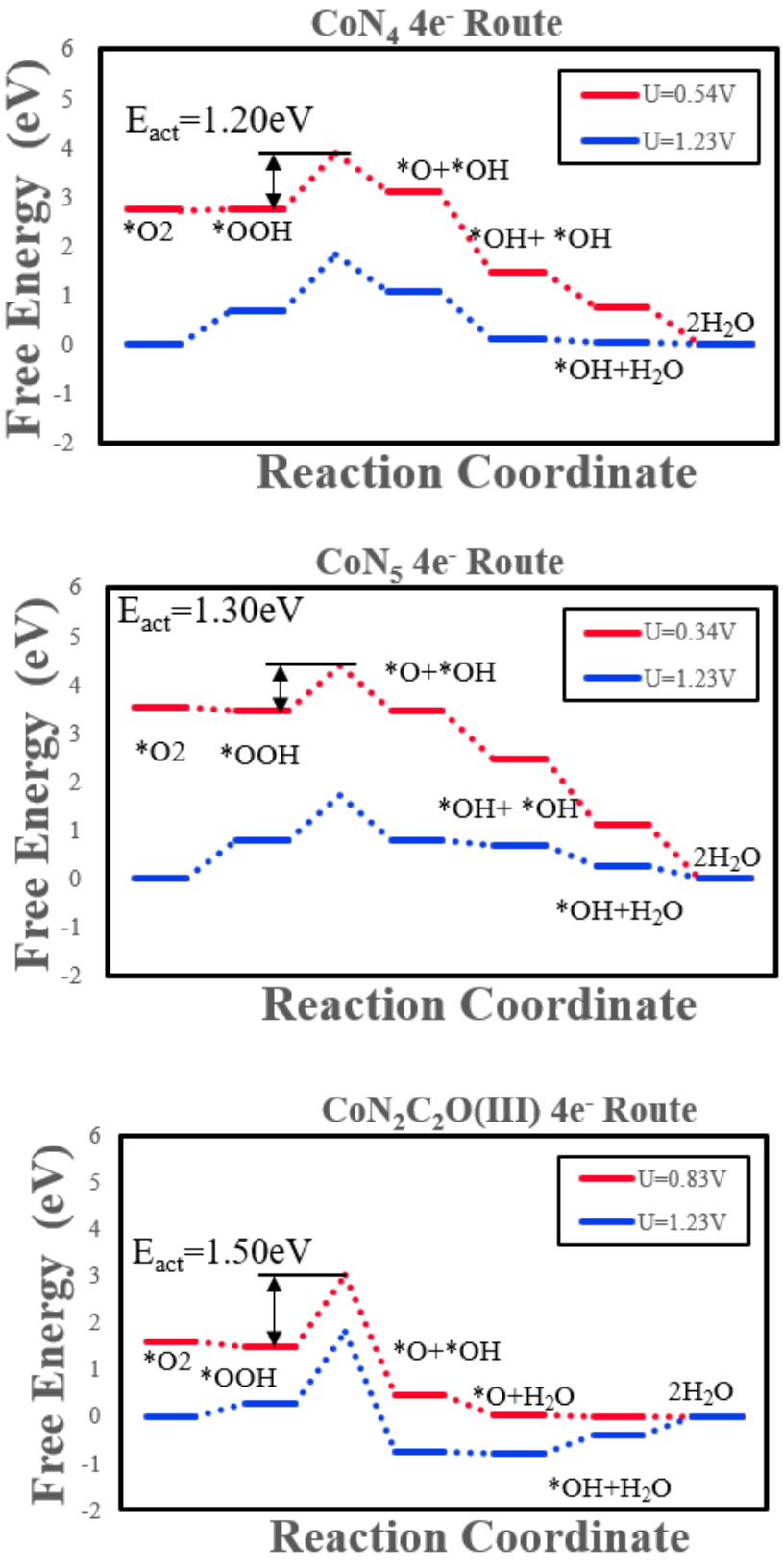

Figure 30. Free energy landscapes of 4e⁻ ORR on CoN_4, CoN_5 and CoN_2C_2O(III) clusters.

In Figure 29 and 30, red lines represent the free energy landscapes at limiting potentials, where the $4e^-$ ORR is still thermodynamically favorable. Blue lines show the free energy landscapes at 1.23V where the free energy levels of the reactants and the product of $4e^-$ ORR are equivalent. By analyzing the free energy landscapes at limiting potentials, the factor that restricts the limiting potential can be found. For CoN_2C_2(I) and CoN_3C clusters, the limiting potentials are restricted by the strong adsorption of O on bridge site. For CoN_4 and CoN_5 clusters, the limiting potentials are restricted by the weak adsorption of OOH. For CoN_2C_2O(III) cluster, the limiting potential is restricted by both the strong adsorption of O on the bridge site and the weak adsorption of OOH.

The active energies acquired by Cl-NEB method for OOH dissociation on CoN_2C_2(I), CoN_3C, CoN_4, CoN_5 and CoN_2C_2O(III) clusters are 0.76eV, 0.95eV, 1.15eV,0.93eV and 1.50 eV, respectively. Due to the polarization on electrode surface, the potential rises along the current density. The cluster with a higher limiting potential are harder to be deactivated when the potential rises. Therefore, an ideal cluster should acquire a low active energy level and a high limiting potential level.

Table 5. Active energies and limiting potentials of $4e^-$ ORR on CoN_2C_2(I), CoN_3C, CoN_4, CoN_5 and CoN_2C_2O(III) clusters.

	CoN_2C_2(I)	CoN_3C	CoN_4	CoN_5	CoN_2C_2O(III)
E_{act}	0.78eV	0.99eV	1.20eV	1.30eV	1.50eV
Limiting potential	0.42V	0.50V	0.55V	0.34V	0.83V

Table 5 gives out an obvious conclusion that though CoN_2C_2O(III) cluster has the highest limiting potential, its huge energy requirement for OOH dissociation makes $4e^-$ ORR hardly happen. The CoN_2C_2(I) cluster with lowest active energy level is the most possible one as the active site on Co-N/C materials.

3.5 SIDE REACTION

Except for the $4e^-$ ORR pathways, the reactant O_2 may be reduced in a $2e^-$-pathway producing hydrogen peroxide with a standard electrode potential at 0.695eV. The free energy evolutions of this side reaction on Co-N_x clusters are plotted in Figure 31 and 32. Similar to the free energy landscapes for 4e- ORR, red lines indicate the free energy landscapes at limiting potential, and the blue lines represent the free energy landscapes when the free energy levels of the reactants and the products are equivalent. Differ from the $4e^-$ ORR, there is not distinct energy barriers along the reaction coordinates since the O-O bonds do not break and the H_2O_2 adsorptions on the clusters are very weak.

Table 6. Limiting potentials of $2e^-$ ORR on CoN_2C_2(I), CoN_3C, CoN_4, CoN_5 and CoN_2C_2O(III) clusters.

	CoN_2C_2(I)	CoN_3C	CoN_4	CoN_5	CoN_2C_2O(III)
Limiting potential(V)	0.47	0.56	0.54	0.42	0.44

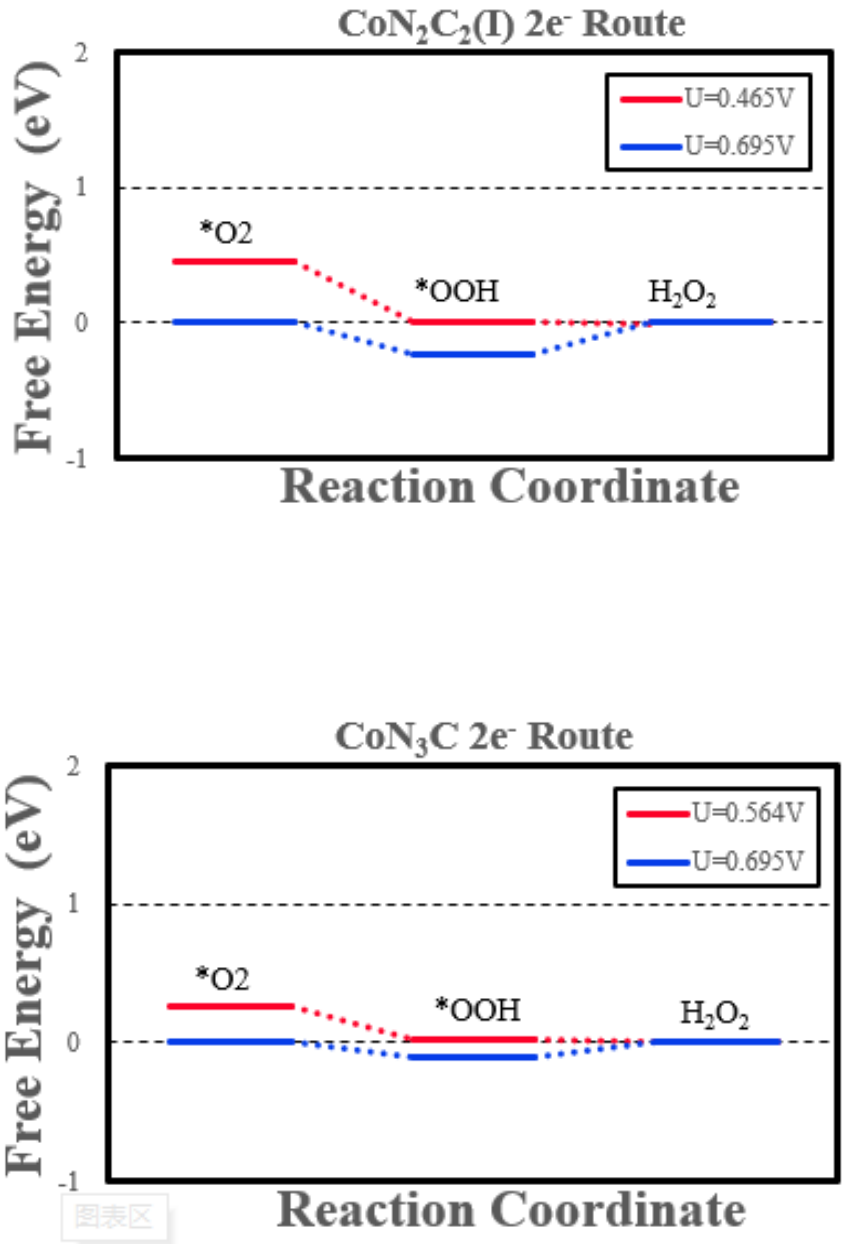

Figure 31. Free energy landscapes of $2e^-$ ORR on CoN_2C_2(I) and CoN_3C clusters.

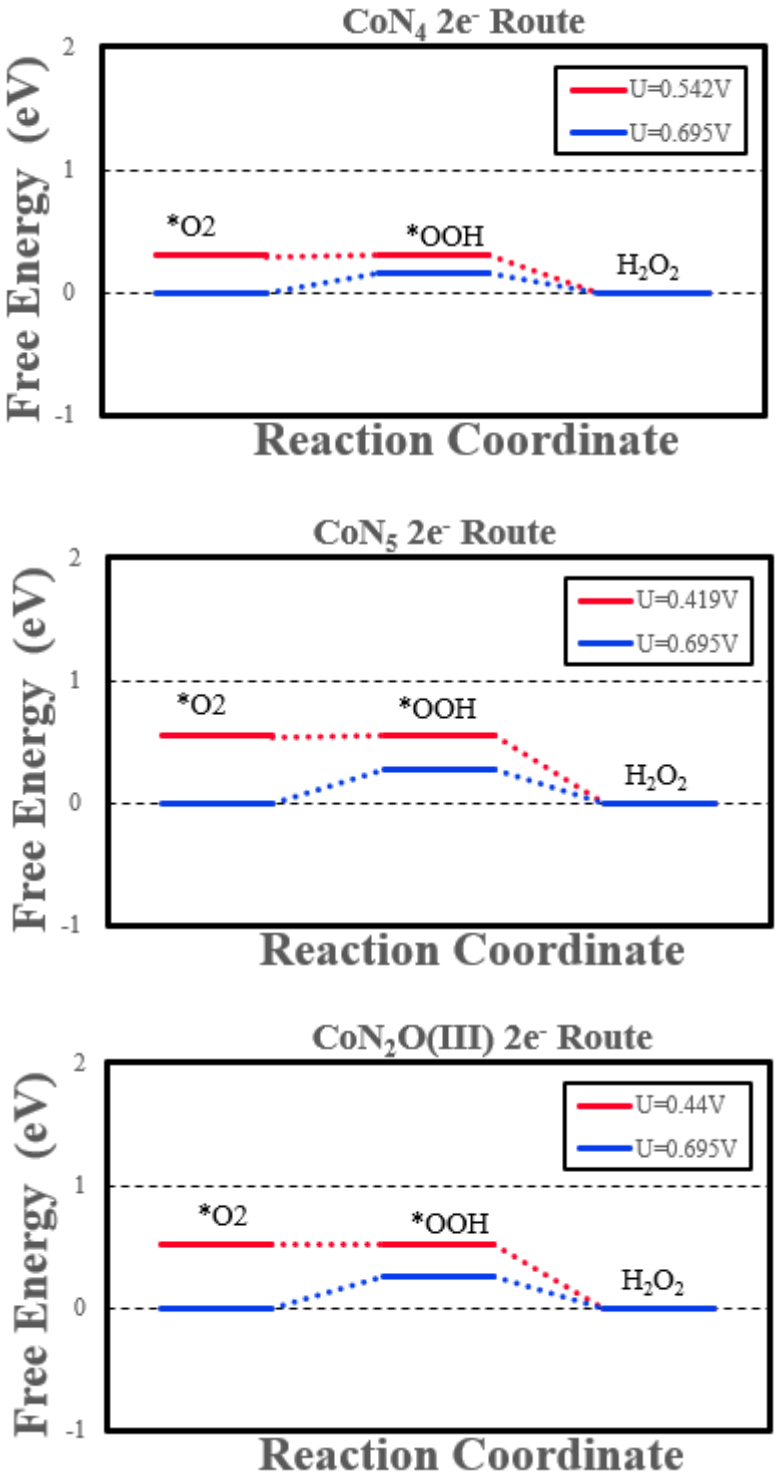

Figure 32. Free energy landscapes of $2e^-$ ORR on CoN_4, CoN_5 and CoN_2C_2O(III) clusters.

The $2e^-$-pathway of ORR consists of O_2 protonation reaction and OOH protonation reaction. All elemental reactions on all CoN_x sites are energetically feasible (downhill in free energy) with low electrode potential. It is observed that the OOH adsorption on CoN_2C_2(I) and CoN_3C clusters is stronger than that on CoN_4 and CoN_5 clusters due to the less number of the surrounding N atoms, decreasing the free energy change in O_2 protonation and increasing the free energy change in OOH protonation. The limiting potentials of $2e^-$-pathway on CoN_x(O) sites are calculated as 0.47V, 0.56V, 0.54V, 0.42V and 0.44V, respectively. Compared to the limiting potential for $4e^-$ ORR pathway on CoN_x clusters shown in the last sector, it is suggested that the $4e^-$ ORR pathway and the $2e^-$ ORR pathway almost share the same limiting potential. The result shows an acceptable selectivity for ORR on CoN_x(O) clusters as the active site of ORR.

The restricting factor of the limiting potential can also be found for $2e^-$ ORR. OOH protonation is the restricting factor on CoN_2C_2(I) and CoN_3C clusters due to the relatively strong OOH adsorption while O_2 protonation is the limiting factor on CoN_4, CoN_5 and CoN_2C_2O(III) clusters because of the relatively weak OOH adsorption.

3.6 DISCUSSION

This study computationally investigates the specific mechanism of ORR on Co-N_x(O) clusters as the active site of nonprecious Co-N/C materials using DFT method.

As shown in Figure 11, 11 models are set to be studied as the possible active site for ORR on Co/N/C materials. The Co atom, expected to be the most crucial functional site, is in the right middle of the models, surrounded by x (x=2, 3, 4, 5) N atoms. In the planar structures of CoN_2C_2(I) and CoN_3C clusters, the central Co atom is also surrounded by 2 or 1 C atom, which

introduces bridge site to the system. The bridge site adsorption of ORR species (such as O and OH) is much stronger than the adsorption on the top site of the central Co atom. This discovery is later believed to be the reason of the varied ORR mechanisms and free energy levels. the strong bridge side adsorption also leads to the assumption of CoN_2C_2O(III) cluster, which has an adsorbed O on the bridge site.

The mechanism study shows the existence of bridge site makes a huge difference on the choice of reaction pathways. In the atomic structures of OOH dissociation products shown in Figure 13, the OH species is adsorbed on an adjacent C atom for CoN_4 and CoN_5 clusters, while the OH species is linked on the central Co atom for CoN_2C_2(I), CoN_3C and CoN_2C_2O(III) clusters. In the next reaction step of O-OH reduction, due to the remarkably strong adsorption of O species on the bridge site, OH protonation is preferred on CoN_2C_2(I), CoN_3C and CoN_2C_2O(III) clusters, and O protonation is more likely to happen on CoN_4 and CoN_5 clusters.

The free energy study for ORR on CoN_x(O) clusters reveals that the $4e^-$ ORR pathway, including the dominating OOH dissociation reaction, is thermodynamically favorable on all Co-N_x(O) sites. Yet the activation energies calculated later in Cl-NEB method implies that the OOH dissociation could hardly occur on CoN_x(O) clusters except for CoN_2C_2(I). Moreover, the comparison of the limiting potentials of the $2e^-$ ORR and the $4e^-$ ORR shows an acceptable selectivity of CoN_x(O) clusters for ORR. Among all discussed clusters, CoN_2C_2(I) is the most possible one as the active site of ORR on Co-N/C materials

In conclusion, the decreasing number of N atoms surrounding the central Co atom does strengthen the adsorption of all ORR species on CoN_x(O) clusters. More distinct differences are caused by the strong bridge adsorption of O. Such strong adsorption decreases the active energy

required by OOH dissociation making the reaction easier to occur. It also restricting the limiting potential, resulting a poor activity at high potential between the electrode and the electrolyte.

4.0 CONCLUSIONS

In summary, this project computationally studies the electrocatalytic activity of $CoN_x(O)$ clusters as the possible active site of nonprecious Co-N/C materials for ORR. The first principles DFT calculations are utilized to investigate the true nature of the active sites and specific mechanisms of ORR on pyrolyzed Co-M/C materials. The active sites are assumed to be a planar structure of $CoN_x(O)$ cluster embedded in graphene as carbon support. Additional O atom on the bridge site is introduced in some models given by the stable state of adsorbed O system. The central Co atom is bound with 2, 3, 4, 5 N atoms, respectively. The adsorption energy study shows that the reactant O_2 could be adsorbed on all $CoN_x(O)$ clusters with reasonable strength to initialize the reaction. the product H_2O is found weakly adsorbed on all Co-$N_x(O)$ clusters, allowing the product to be released easier from the catalyst surface. Further studies of free energy calculations suggest that the $4e^-$ ORR pathway is thermodynamically favorable on all $CoN_x(O)$ clusters. The active energy calculation indicates that $CoN_2C_2(I)$ cluster has the lowest active energy of 0.78eV, very close to the high performance FeN_4 cluster which has the active energy of 0.69eV reported by previous studies. The 2e- ORR analyses also show the acceptable selectivity of all $CoN_x(O)$ clusters for ORR. These results all support that both $2e^-$ ORR and $4e^-$ORR can occur on Co-N/C materials which matches with the experimental result.

In mechanism study, the O species is adsorbed on the bridge site at the final state of OOH dissociation reaction on $CoN_2C_2(I)$ and CoN_3C clusters due to the strong bridge site adsorption

of O species. For the same reason, OH protonation is more favorable on the two clusters in O-OH reduction reaction, while CoN_4 and CoN_5 clusters prefers O protonation.

The lack of N atoms makes CoN_2C_2(I) and CoN_3C clusters show a stronger adsorption for all ORR species, it also allows the existence of bridge site, which demonstrates an even stronger adsorption for O and weaker adsorption for OH. This strong adsorption is found limiting some elemental reactions of $4e^-$ ORR pathway. After all, the CoN_2C_2(I) cluster is the most possible cluster as the active site that conducts both $2e^-$ and $4e^-$ ORR.

APPENDIX A

ZPE CORRECTIONS AND ENTROPIC CONTRIBUTIONS

Table 7. ZPE corrections and entropic contributions to the free energies (from ref 22).

	TS	TΔS	ZPE	ΔZPE	ΔZPE- TΔS
H_2O	0.67	0	0.56	0	0
$^*OH+1/2H_2$	0.20	-0.47	0.44	-0.12	0.35
$^*O+H_2$	0.41	-0.27	0.34	-0.22	0.05
$1/2O_2+H_2$	0.73	0.05	0.32	-0.24	-0.29
H_2	0.41		0.27		
$1/2O_2$	0.32		0.05		
$^*O$	0		0.07		
$^*OH$	0		0.30		
$^*H$	0		0.17		

.

APPENDIX B

FILES USED IN VASP

VASP is a commercial code pack to conduct DFT calculations. To operate it, four files are needed:

POSCAR contains the lattice parameters of a unit cell and the locations of all atoms in it.

POTCAR contains the pseudopotential parameters of all elements existing in POSCAR.

KPOINTS determines the sample points in Brillouin zone.

INCAR contains all other parameters that involve in the calculation.

To obtain the configuration of a steady state and its relative energy without entropy, all those four files needs to be edited. For example, the four files used for CoN4 cluster in this study are attached below.

B.1 POSCAR

```
Co N C
   1.00000000000000
     9.8428295798363301     0.0000000000000000     0.0000000000000000
     0.0000000000000000     8.5241404612591740     0.0000000000000000
     0.0000000000000000     0.0000000000000000    14.0000000000000000
   1   4  26
Direct
  0.4999994840052935  0.5833309336047350  0.0051063319192863
  0.3685907097688599  0.7454518864540347  0.0032620323583004
  0.6314085833989083  0.4212162845935978  0.0032615887104015
  0.3685907337358714  0.4212149796557938  0.0032610719517479
  0.6314093796924070  0.7454532307214379  0.0032632509014903
  0.9999992594320375  0.0001467842840057  0.9987956993949965
  0.8751421416562479  0.2489826697908910  0.9994315164592891
  0.3741894099891425  0.2569317037011629  0.0027978151325669
  0.7540772897006534  0.4988779211658283  0.0011911159168747
  0.2459233985365827  0.4988759746257401  0.0011898295356190
  0.1233982425403610  0.7503436863822017  0.9993411218678574
  0.2509847285517353  0.9987164614117958  0.0009964252650576
  0.7490137078753563  0.9987169892791741  0.0009971161666229
  0.1248593177608086  0.2489836979366800  0.9994306955539898
  0.6258104959869542  0.2569281157228929  0.0027981641039290
  0.0000016244737964  0.5004382937358827  0.9986722713010181
  0.8765998011699452  0.7503451149635936  0.9993412810514570
  0.9999990068359779  0.1665201246969445  0.9987950742738931
  0.8765991234863861  0.4163205054117043  0.9993408231964764
  0.7540767296234137  0.6677901572989029  0.0011920182633887
  0.2459228088705316  0.6677909967122915  0.0011903471725390
  0.6258107999662954  0.9097378377587049  0.0027995879763907
  0.1248600240240521  0.9176817870154395  0.9994325849526859
  0.2509845863889666  0.1679497410100481  0.0009959071989982
  0.7490147841224228  0.1679502442666134  0.0009971944365574
  0.1233992775981534  0.4163216960090352  0.9993394609276578
  0.0000018593362867  0.6662295164470109  0.9986728232279489
  0.8751413334309461  0.9176835166725610  0.9994324730374089
  0.3741901204001934  0.9097379519646864  0.0027982187420150
  0.5000005326144290  0.1709383091659546  0.0034480786797744
  0.5000007050269986  0.9957262208738982  0.0034474127991473
```

B.2 POTCAR

POTCAR files for each element are provided within VASP. A POTCAR file for a cluster is a simple superposition of the POTCAR files of the elements that make up the cluster. POTCAR files are very large, even for a single element. Only a few rows of the POTCAR file for H element used in this study are demonstrated here.

```
PAW_PBE H 15Jun2001
 1.00000000000000000
 parameters from PSCTR are:
   VRHFIN =H: ultrasoft test
   LEXCH  = PE
   EATOM  =    12.4884 eV,     .9179 Ry

   TITEL  = PAW_PBE H 15Jun2001
   LULTRA =        F    use ultrasoft PP ?
   IUNSCR =        0    unscreen: 0-lin 1-nonlin 2-no
   RPACOR =     .000    partial core radius
   POMASS =    1.000; ZVAL   =    1.000    mass and valenz
   RCORE  =    1.100    outmost cutoff radius
   RWIGS  =     .700; RWIGS  =     .370    wigner-seitz radius (au A)
   ENMAX  =  250.000; ENMIN  =  200.000 eV
   RCLOC  =     .701    cutoff for local pot
   LCOR   =        T    correct aug charges
   LPAW   =        T    paw PP
   EAUG   =  400.000
   RMAX   =    2.174    core radius for proj-oper
   RAUG   =    1.200    factor for augmentation sphere
   RDEP   =    1.112    radius for radial grids
   QCUT   =   -5.749; QGAM   =   11.498    optimization parameters

   Description
     l     E      TYP  RCUT    TYP  RCUT
     0   .000     23  1.100
     0   .500     23  1.100
     1  -.300     23  1.100
   Error from kinetic energy argument (eV)
   NDATA  =      100
   STEP   =   20.000   1.050
  5.77      5.50      5.37      5.11      4.99      4.75      4.52      4.40
  4.19      3.98      3.88      3.68      3.49      3.31      3.14      2.98
  2.83      2.68      2.54      2.35      2.22      2.11      1.94      1.84
```

```
  1.74      1.61      1.48      1.40      1.29      1.19      1.09      1.01
  .925      .851      .782      .719      .642      .590      .526      .482
  .430      .382      .339      .301      .267      .236      .209      .178
  .157      .133      .113      .988E-01  .832E-01  .697E-01  .562E-01  .467E-01
  .386E-01  .305E-01  .239E-01  .186E-01  .143E-01  .109E-01  .820E-02  .580E-02
  .425E-02  .291E-02  .195E-02  .130E-02  .808E-03  .544E-03  .368E-03  .278E-03
  .239E-03  .227E-03  .225E-03  .224E-03  .218E-03  .204E-03  .181E-03  .156E-03
  .127E-03  .983E-04  .735E-04  .520E-04  .369E-04  .274E-04  .225E-04  .204E-04
  .201E-04  .200E-04  .193E-04  .178E-04  .151E-04  .121E-04  .914E-05  .676E-05
  .512E-05  .437E-05  .412E-05  .410E-05
END of PSCTR-controll parameters
 local part
 170.075338972103111
   .24362014E+01   .24358776E+01   .24349034E+01   .24332803E+01   .24310092E+01
        ⋮
```

B.3 INCAR

```
SYSTEM = CoN4
 Start parameters for this run:
   ISTART = 0
   ICHARG = 2

 Electronic relaxation:
   ISMEAR = -1
   SIGMA  = 0.025
   PREC   = Accurate
   ADDGRID = .TRUE.
   EDIFF  = 1E-6
   NELM   = 200
   ENCUT  = 400
   ISPIN  = 2
   MAGMOM = 1*3 4*3 26*2
   NPAR   = 8

   GGA    = RP

   ALGO   = N
   LREAL  = Auto

 Ionic relaxation:
```

```
   NSW    = 150
   IBRION = 2
   ISIF   = 2
   EDIFFG = -0.01
   LDIPOL = .TRUE.
   IDIPOL = 3

 Output:
   LCHARG = .FALSE.
   LWAVE  = .FALSE.
   LORBIT = 11
```

B.4 KPOINTS

```
k-point
0
g
4  4  1
0  0  0
```

BIBLIOGRAPHY

1. Züttel, A. Hydrogen storage methods. *Naturwissenschaften* **91,** 157–172 (2004).

2. Albritton, D. L. *et al.* Core Writing Team Climate Change 2001: Synthesis Report. (2001).

3. Jochem, E. Long-Term Potentials of Rational Energy use - The Unknown Possibilities of Reducing Greenhouse Gas Emissions. *Energy Environ.* **2,** 31–44 (1991).

4. Eia. Annual Energy Outlook 2017 with projections to 2050. (2017).

5. Lewis, N. S. & Nocera, D. G. Powering the planet: Chemical challenges in solar energy utilization. *Proc. Natl. Acad. Sci.* **103,** 15729–15735 (2006).

6. Debe, M. K. Electrocatalyst approaches and challenges for automotive fuel cells. *Nature* **486,** 43–51 (2012).

7. Hydrogen energy — Abundant, efficient, clean: A debate over the energy-system-of-change. *Int. J. Hydrogen Energy* **34,** S1–S52 (2009).

8. Steele, B. C. H. & Heinzel, A. Materials for fuel-cell technologies. *Nature* **414,** 345–352 (2001).

9. Mehta, V. & Cooper, J. S. Review and analysis of PEM fuel cell design and manufacturing. *J. Power Sources* **114,** 32–53 (2003).

10. Chen, Z., Higgins, D., Yu, A., Zhang, L. & Zhang, J. A review on non-precious metal electrocatalysts for PEM fuel cells. *Energy Environ. Sci.* **4,** 3167 (2011).

11. JASINSKI, R. A New Fuel Cell Cathode Catalyst. *Nature* **201,** 1212–1213 (1964).

12. Franke, R., Ohms, D. & Wiesener, K. Investigation of the influence of thermal treatment on the properties of carbon materials modified by N4-chelates for the reduction of oxygen in acidic media. *J. Electroanal. Chem. Interfacial Electrochem.* **260,** 63–73 (1989).

13. Baker, R., Wilkinson, D. P. & Zhang, J. Electrocatalytic activity and stability of substituted iron phthalocyanines towards oxygen reduction evaluated at different temperatures. *Electrochim. Acta* **53,** 6906–6919 (2008).

14. Chung, H. T., Won, J. H. & Zelenay, P. Active and stable carbon nanotube/nanoparticle composite electrocatalyst for oxygen reduction. *Nat. Commun.* **4,** 1922 (2013).

15. Parvez, K. *et al.* Nitrogen-Doped Graphene and Its Iron-Based Composite As Efficient Electrocatalysts for Oxygen Reduction Reaction. *ACS Nano* **6,** 9541–9550 (2012).

16. Wu, G., More, K. L., Johnston, C. M. & Zelenay, P. High-Performance Electrocatalysts for Oxygen Reduction Derived from Polyaniline, Iron, and Cobalt. *Science (80-.).* **332,** 443–447 (2011).

17. Li, Y. *et al.* An oxygen reduction electrocatalyst based on carbon nanotube–graphene complexes. *Nat. Nanotechnol.* **7,** 394–400 (2012).

18. Liu, K., Kattel, S., Mao, V. & Wang, G. Electrochemical and Computational Study of Oxygen Reduction Reaction on Nonprecious Transition Metal/Nitrogen Doped Carbon Nanofibers in Acid Medium. *J. Phys. Chem. C* **120,** 1586–1596 (2016).

19. Bashyam, R. & Zelenay, P. A class of non-precious metal composite catalysts for fuel cells. *Nature* **443,** 63–66 (2006).

20. Lefèvre, M., Proietti, E., Jaouen, F. & Dodelet, J.-P. Iron-Based Catalysts with Improved Oxygen Reduction Activity in Polymer Electrolyte Fuel Cells. *Science (80-.).* **324,** 71–74 (2009).

21. Zitolo, A. *et al.* Identification of catalytic sites in cobalt-nitrogen-carbon materials for the oxygen reduction reaction. *Nat. Commun.* **8,** 957 (2017).

22. Nørskov, J. K. *et al.* Origin of the Overpotential for Oxygen Reduction at a Fuel-Cell Cathode. *J. Phys. Chem. B* **108,** 17886–17892 (2004).

23. Viswanathan, V., Hansen, H. A., Rossmeisl, J. & Nørskov, J. K. Universality in Oxygen Reduction Electrocatalysis on Metal Surfaces. *ACS Catal.* **2,** 1654–1660 (2012).

24. Kattel, S. & Wang, G. A density functional theory study of oxygen reduction reaction on Me–N4 (Me = Fe, Co, or Ni) clusters between graphitic pores. *J. Mater. Chem. A* **1,** 10790 (2013).

25. Lee, D. H., Lee, W. J., Lee, W. J., Kim, S. O. & Kim, Y.-H. Theory, Synthesis, and Oxygen Reduction Catalysis of Fe-Porphyrin-Like Carbon Nanotube. *Phys. Rev. Lett.* **106,** 175502 (2011).

26. Kattel, S. & Wang, G. Reaction Pathway for Oxygen Reduction on FeN_4 Embedded Graphene. *J. Phys. Chem. Lett.* **5,** 452–456 (2014).

27. Zhang, J., Vukmirovic, M. B., Sasaki, K., Uribe, F. & Adzic, R. R. Platinum monolayer electrocatalysts for oxygen reduction: Effect of substrates, and long-term stability. *J. Serbian Chem. Soc.* **70,** 513–525 (2005).

28. Zhang, J., Wang, Z. & Zhu, Z. A density functional theory study on oxygen reduction reaction on nitrogen-doped graphene. *J. Mol. Model.* **19,** 5515–5521 (2013).

29. Su, Y. *et al.* Cobalt nanoparticles embedded in N-doped carbon as an efficient bifunctional electrocatalyst for oxygen reduction and evolution reactions. *Nanoscale* **6,** 15080–15089 (2014).

30. Wang, X. X. *et al.* Nitrogen-Coordinated Single Cobalt Atom Catalysts for Oxygen Reduction in Proton Exchange Membrane Fuel Cells. *Adv. Mater.* 1706758 (2018). doi:10.1002/adma.201706758

31. Kresse, G. & Hafner, J. *Ab initio* molecular dynamics for liquid metals. *Phys. Rev. B* **47,** 558–561 (1993).

32. Kresse, G. & Furthmüller, J. Efficiency of ab-initio total energy calculations for metals and semiconductors using a plane-wave basis set. *Comput. Mater. Sci.* **6,** 15–50 (1996).

33. Hohenberg, P. & Kohn, W. Inhomogeneous Electron Gas. *Phys. Rev.* **136,** B864–B871 (1964).

34. Kohn, W. & Sham, L. J. Self-Consistent Equations Including Exchange and Correlation Effects. *Phys. Rev.* **140,** A1133–A1138 (1965).

35. Hammer, B., Hansen, L. B. & Nørskov, J. K. Improved adsorption energetics within density-functional theory using revised Perdew-Burke-Ernzerhof functionals. *Phys. Rev. B* **59,** 7413–7421 (1999).

36. Kresse, G. & Joubert, D. From ultrasoft pseudopotentials to the projector augmented-wave method. *Phys. Rev. B* **59,** 1758–1775 (1999).

37. Blöchl, P. E. Projector augmented-wave method. *Phys. Rev. B* **50,** 17953–17979 (1994).

38. Monkhorst, H. J. & Pack, J. D. Special points for Brillouin-zone integrations. *Phys. Rev. B* **13,** 5188–5192 (1976).

39. Sheppard, D., Terrell, R. & Henkelman, G. Optimization methods for finding minimum energy paths. *J. Chem. Phys.* **128,** (2008).

40. Henkelman, G., Uberuaga, B. P. & Jónsson, H. A climbing image nudged elastic band method for finding saddle points and minimum energy paths. *J. Chem. Phys.* **113,** 9901–9904 (2000).

41. Henkelman, G. & Jónsson, H. A dimer method for finding saddle points on high dimensional potential surfaces using only first derivatives. *J. Chem. Phys.* **111,** 7010–7022 (1999).

42. Duan, Z. & Wang, G. A first principles study of oxygen reduction reaction on a Pt(111) surface modified by a subsurface transition metal M (M = Ni, Co, or Fe). *Phys. Chem. Chem. Phys.* **13,** 20178 (2011).

43. Duan, Z. & Wang, G. Comparison of reaction energetics for oxygen reduction reactions on Pt(100), Pt(111), Pt/Ni(100), and Pt/Ni(111) surfaces: A first-principles study. *J. Phys. Chem. C* **117,** 6284–6292 (2013).

44. Greeley, J. *et al.* Alloys of platinum and early transition metals as oxygen reduction electrocatalysts. *Nat. Chem.* **1,** 552–556 (2009).